ELECTRO-OPTICAL AND INFRARED DESIGN FOR UNCREWED AERIAL SYSTEM COLLISION AVOIDANCE

by

Richard Cavanaugh

A Thesis Submitted to the Faculty of the

WYANT COLLEGE OF OPTICAL SCIENCES

In Partial Fulfillment of the Requirements

For the Degree of

MASTER OF SCIENCE

In the Graduate College

THE UNIVERSITY OF ARIZONA

2024

THE UNIVERSITY OF ARIZONA
GRADUATE COLLEGE

As members of the Master's Committee, we certify that we have read the thesis prepared by **Richard Colton Cavanaugh,** titled ***Electro-Optical and Infrared System Design for Uncrewed Aerial System Collision Avoidance*** and recommend that it be accepted as fulfilling the thesis requirement for the Master's Degree.

Professor Ronald G. Driggers Date: May 2, 2024

Professor Florian Willomitzer Date: May 2nd, 2024

Professor David Brady Date: 2 May 2024

Final approval and acceptance of this thesis is contingent upon the candidate's submission of the final copies of the thesis to the Graduate College.

I hereby certify that I have read this thesis prepared under my direction and recommend that it be accepted as fulfilling the Master's requirement.

Professor Ronald G. Driggers Date: May 2, 2024
Master's Thesis Committee Chair
Wyant College of Optical Sciences

ACKNOWLEDGEMENTS

Thank you, first and foremost, to SARA (Scientific Applications & Research Associates) for their financial support of this research. Without your support, this work would not have been possible.

To Dr. Ronald Driggers and my peers in the Infrared Systems Research Group at the University of Arizona: Thank you for your patience, kindness, and support throughout my MS career. Ron, you are an incredible mentor to your students – you never fail to keep it simple, keep it real, and keep it kind. And, for young people navigating a confusing world and time of life, that is an enormous blessing.

To Dr. Patrick Leslie and Dr. Lindsey Wiley: You were both so generous in welcoming me as your colleague, despite my lack of background, and you offered nothing but patience and understanding as I learned the ropes. You helped me feel welcome, seen, and at ease in this program. I admire you both as brilliant researchers and great people, and I feel lucky to have met you both.

To Dr. Brian Anderson: Thank you for working with me as I prepared to apply for this MS program, and for your ongoing support since then. Without your open-minded support in those early days, I would not be here. I am so grateful for your ongoing support; it really does mean so much.

To my many mentors at Loyola Marymount University, Dr. Vandana Thadani, Dr. Mairead Sullivan, Dr. Erin Stackle, Dr. Anna Muraco, Dr. Andrew Dilts, Dr. Jeniffer Williams, Dr. Alexandra Neal… And so many others. Each of you taught me invaluable lessons: how to care with my whole heart and mind, how to think critically and with kindness, how to fight for what is right, how to dream, how to trust and take care of myself, and how to be free. I will carry these lessons and so many others with me everywhere I go!

To my queer community around the world: You are the light that sustains me and guides my growth. Thank you for your resilience, love, ingenuity, kindness, style, and wisdom. A special and heartfelt thank you to Kyte Fehlau and Rosa de la Rosa – you are an endless inspiration to me and a treasure of my heart.

To Trevor: I met you halfway through this program, when I was struggling to find my community and sense of purpose in Tucson. Getting to know you has been such a joy – your endless creativity and zest for life inspires me every day, and it has brought so much beauty and balance to my life. You have made Tucson feel like home.

To my family: Thank you for offering your unfailing love and support throughout the years. No matter how I am feeling, you remind me that I can accomplish whatever I set my mind to. And, more importantly, you remind me that I am free to set my mind to whatever I desire. You make me feel safe to challenge myself to grow.

And to my readers: I acknowledge that The University of Arizona is on the land and territories of Indigenous peoples. Today, Arizona is home to 22 federally recognized tribes, with Tucson being home to the O'odham and the Yaqui. As much as we should commend and support efforts made by the University and other Arizona institutions for their efforts to collaborate with and support Indigenous communities, we must remain aware that very real people continue to bear the burden of historical colonialist trauma. And we must remain aware that this trauma is, in so many ways, ongoing. Allow this truth to make a place in your heart, and let it guide your conscience as you connect and engage with your community in Tucson and elsewhere.

“The most beautiful dream that has haunted the heart of man since Icarus is today reality.”

Louis Blériot

“Icarus had a sister, for whom no name will serve. She who is lost now forever in the labyrinth of the world.”

J.M. Coetzee

TABLE OF CONTENTS

LIST OF FIGURES

LIST OF FIGURES – *Continued*

LIST OF TABLES

List of Abbreviations

AAM	Advanced Air Mobility
ACAS X/Xa/Xu	Airborne Collision Avoidance System X/Xa/Xu
ACE-O	Acoustically-Cued Electro-Optic
ADC	Analog-to-Digital Converter
ADS-B	Automatic Dependent Surveillance-Broadcast
ASTM	American Society for Testing and Materials
ATC	Air Traffic Control
AV	Allied Vision
BLIP	Background Limited Infrared Photodetection
BVLOS	Beyond Visual Line Of Sight
C172/C182	Cessna 172/182
C2	Command and Control
CAR	Civil Air Regulations
CCD	Charge-Coupled Device
CMOS	Complementary Metal-Oxide-Semiconductor
CTIA	Capacitive TransImpedance Amplifier
CTF	Contrast Threshold Function
DAA	Detect and Avoid
DI	Direct Injection readout circuit
EO/IR	Electro-optical and Infrared

eSWIR	extended-Shortwave Infrared Band (2 to 2.4 microns)
FAA	Federal Aviation Administration
FAR	Federal Aviation Regulations
FLIR	Forward-Looking InfraRed
FMRA	FAA Modernization and Reform Act
FOV	Field of View
GA	General Aviation
GaSb	Gallium Antimonide
GSD	Ground Sample Distance
HFOV	Horizontal Field of View
HgCdTe (MCT)	Mercury Cadmium Telluride
IFOV	Instantaneous field of view
IFR	Instrument Flight Rules
InGaAs	Indium Gallium Arsenide
InSb	Indium Antimonide
LiDAR	Light Detection and Ranging
LTI	Linear, Time-Invariant system
LWIR	Longwave Infrared Band (8 to 14 microns)
MODTRAN	MODerate resolution atmospheric TRANsmission model
MTF	Modulation Transfer Function
MUX	Multiplexer
MWIR	Midwave Infrared Band (3 to 5 microns)

NAS	U.S. National Airspace
NEP	Noise-Equivalent Power
NETD	Noise-Equivalent Temperature Difference
NextGen	Next Generation Air Transportation System
NIR	Near-Infrared Band (0.7 to 1 microns)
NMAC	Near Mid-Air Collision
NVIPM	Night Vision Integrated Performance Model
PANCAS	Passive Acoustic Non-cooperative Collision Avoidance System
PbS	Lead Sulfide
PbSe	Lead Selenide
PM	Particulate Matter
POT	Pixels on Target
PSF	Point-Spread Function
PSR	Primary Surveillance Radar
QE	Quantum Efficiency
RGB	Red-Green-Blue
ROI	Region of Interest
ROIC	Readout Integrated Circuit
RPA	Remotely Piloted Aircraft
RSS $\Delta R/\Delta T$	Root-Sum-Squared Delta Reflectivity/Temperature
SITF	System Intensity Transfer Function
SNR	Signal-to-Noise Ratio
SSR	Secondary Surveillance Radar

sUAS	Small Uncrewed Aerial System
SWaP	Size, Weight, and Power
SWIR	Shortwave Infrared Band (1 to 1.7 microns)
TCAS	Traffic Alert and Collision Avoidance System
T2SL	Type-II Superlattice
TTP	Targeting Task Performance
UAS/UAV	Uncrewed Aerial System/Uncrewed Aerial Vehicle
UTM	UAS Traffic Management
VFR	Visual Flight Rules
VIS	Visible Band (0.4 to 0.7 microns)
VOx	Vanadium Oxide

List of Symbols

α	calibration constant
A_d	detector area
C_{tgt}	apparent contrast
D	aperture diameter
D^*	dee-star, detectivity
d_{Airy}	optical spot diameter (image plane)
d_{det}	detector pitch
ε	epsilon, emissivity
F / $F\#$	f-number
f	focal length
Δf	delta f, spectral bandwidth
I	intensity
J_1	first-order Bessel function
λ	lambda, wavelength
L_{tgt}	target characteristic dimension
μ_{tgt}	mu-target, mean signal on target in gray values
μ_{bck}	mu-background, mean signal of background in gray values
M	emittance
Φ	phi, flux
R	range
σ	sigma, noise
σ_{tgt}	sigma-target, standard deviation of signal on target in gray values
S_{tmp}	scene temperature resulting in average display luminance
τ	tau, time constant

T	temperature
θ_{min}	theta-min, optical spot radius (radians)
V	effective cycles on target
V_{50}	vee-50, task difficult metric in effective cycles on target

DISCLOSURES

Chapter 3, “EO/IR Band Comparison of Aircraft-Sky Contrast & Range Performance Simulations,” is a reproduction (with minor edits) of a paper under review for publication in Applied Optics.

ABSTRACT

In recent decades, uncrewed aerial vehicle (UAV) technology has undergone repeated rapid advancements, enabling novel applications in civil, commercial, and scientific projects. Implementing UAV operations in each of these contexts requires the development of thorough safety systems for traffic management and collision avoidance. This is particularly true for beyond visual line-of-sight (BVLOS) operations, which require automated Detect and Avoid (DAA) Systems to recognize collision threats and direct avoidance maneuvers when necessary. EO/IR sensors are commonly employed by DAA systems, providing a low-weight and low-power means for capturing high resolution imagery of surrounding airspace.

This thesis begins with a review of the history of the aircraft collision avoidance problem followed by an introduction to EO/IR system design. The historical review provides relevant regulatory and technological background for optical engineers who may be unaware of the context surrounding DAA technology. The technical review, then, provides DAA researchers who may be more familiar with other system components or sensing modalities with the necessary optical background to appreciate the contribution of the EO/IR study. After this introduction, plane-to-sky contrast is compared in the VIS (0.4 to 0.7 μm), SWIR (1 to 1.7 μm), MWIR (3 to 5 μm), and LWIR (8 to 14 μm) to determine which band is most sensitive to a C182 general aviation aircraft signal against a clear sky background. Contrast in the two reflective bands (VIS and SWIR) is determined in terms of equivalent reflectivity, and contrast in the two emissive bands (MWIR and LWIR) is determined in terms of equivalent blackbody temperature. Sensitivity data is then used alongside resolution specifications to estimate detection range performance using the Night Vision Integrated Performance Model (NVIPM). Results are extrapolated to a maritime atmosphere using the MODerate resolution atmospheric TRANsmission model (MODTRAN). The analysis of contrast, detection range-performance, and recommendations on band selection are provided for reference in the design of EO/IR systems for aircraft collision avoidance. Future research may study band performance at night, against other backgrounds (e.g. clouds, ocean, ground terrain), and over different elevation angles (±15° degrees).

CHAPTER 1

A History of the Collision Avoidance Problem

1.1. Aircraft Collision Avoidance in the 20th Century

Aircraft collision avoidance has been a priority for pilots, aviation companies, and government authorities since the invention of the airplane at the turn of the 20th century. In the decades following the first successful aircraft flight in 1903, air traffic safety was managed by the small aviation companies who designed, tested, and sold the first airplanes. Pilot safety regulations were then modeled after marine practices, focusing on aircraft light requirements and pilot visibility. The efforts of aviation researchers and corporations to safeguard pilot safety mostly focused on decreasing the complexity of cockpit instrument panels and developing multipurpose instruments which would facilitate the pilot's ability to focus more attention on surrounding airspace. Pilots relied on magnetic compasses for navigation, and they flew no higher than 500 feet above ground to track roads and railways. These and other technological limitations meant collisions were commonplace and often fatal [1].

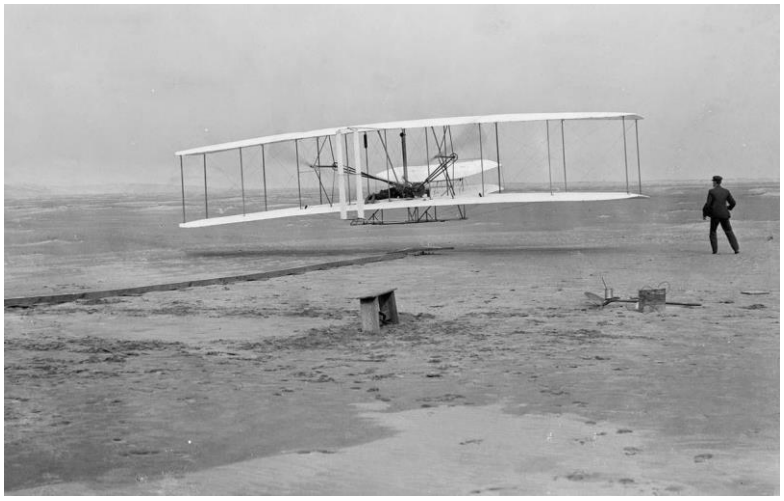

Figure 1.1. The world's first functional aircraft was engineered by Orville and Wilbur Wright. This photograph records its first successful flight in Kitty Hawk, North Carolina on December 17th, 1903 [2].

A lack of consistent and integrated safety regulations increased the likelihood of collisions. In 1919, the European-sponsored International Convention for Air Navigation proposed "rules of the road" which aimed to mitigate the risk of midair collisions and to provide some basis for the development of more thorough systems of air traffic control [3]. By the late 1920's, a commercial airline industry had been established in the United States, and major air transport companies began to advocate for the establishment of US federal safety standards. Industry's call for federal action was answered in 1926, when the Air Commerce Act charged the Secretary of Commerce with promoting air commerce, establishing air safety regulations, and formalizing the certification of aircraft and pilots [3].

In the years following the enactment of the Air Commerce Act, federal aviation authorities encouraged major airlines to collaborate in establishing the first radio-equipped air traffic control centers. Air Traffic Control (ATC) towers enabled radio dispatchers to transmit to airline aircraft up to 50 miles from their terminal airport. This development marked a significant advance in the ability of ground-based operators to manage air traffic, allowing operators to issue detailed procedural instructions to maintain separation between aircraft [3].

Figure 1.2. [Left] A 1930 photograph of the first radio-equipped control tower at the Cleveland Municipal Airport. [Right] Early air traffic controllers tracking aircraft with 'shrimp boats' on a tabletop map [2].

The continued development and operation of ATC centers soon became federal responsibilities, coming under the purview of the Bureau of Air Commerce in 1936 [2]. And soon after, the Civil Aeronautics Act of 1938 provided a new federal regulatory code for air traffic: the Civil Air Regulations (CAR) [3]. Under the CAR, a first generation of formal, federal-level air traffic safety efforts pioneered the development of ATC procedures, new equipment, and facilities for air safety. Included in these procedures were the first contact flight rules (CFR), which would later become visual flight rules (VFR) and instrument flight rules (IFR) [3].

In the 1940s, rapid developments in aviation technology (including the advent of commercial jets) and the consequent rise in air traffic following World War II outpaced evolving safety efforts. In 1956, a Trans World Airlines Super Constellation and United Air Lines DC-7 collision over the Grand Canyon, Arizona killed all 128 occupants of the two planes. Prompted by public dismay over this incident, the Federal Aviation Act was passed in 1958. This act created an independent Federal Aviation Agency (which would later become the Federal Aviation Administration, or FAA) to oversee the safe and efficient use of national airspace [4]. Similar but distinct events throughout the mid-20th century contributed to the gradual unification of airspace rules under federal and international agencies worldwide [5].

WEATHER
Forecast for Tucson and vicinity: Clear.
Temperatures
Yesterday: HIGH 96 LOW 69
Year Ago: HIGH 97 LOW 76
U. S. Weather Bureau

The Arizona Daily Star

★ An Independent NEWSpaper Printing The News Impartially ★

FINAL EDITION
SEVEN CENTS

VOL. 115 NO. 184 TUCSON, ARIZONA, MONDAY MORNING, JULY 2, 1956 TWENTY-TWO PAGES

AIRLINERS COLLIDE; 128 DIE

Politics In Arizona

Pima County Tripped Maricopa Aspirants

By LESTER N. INSKEEP

Pima County took the lead Saturday in a last-minute move that kept Maricopa County from having all three top Democratic political posts in Arizona.

With almost one-half of the total vote in the state, Maricopa already has the positions of Democratic state chairman, held by Dr. J. N. Harber, and national committeeman, held by Stephen W. Langmade, who was re-elected Saturday on motion of Dick Jenkins, chairman of the Pima County Democratic Central Committee.

Where Giant Planes Crashed And Burned

Arrow at left points to the burned spot at the base of the butte by the Colorado River where a TWA Super-Constellation fell in flames killing all 70 aboard Saturday. Other arrow indicates spot on butte where the United Air Lines DC7 crashed, killing 58. The closeness of the two crashed airliners indicates, Air Force officers said, that the two planes collided in air. Helicopters will attempt to bring the bodies of crash victims out of the gorge today. (AP Wirephoto)

Burned Wreckage Found On Peaks In Grand Canyon

U.S. Moves Into Steel Strike

But Union Chieftain Unaware Of Action

PITTSBURGH, July 1 (P)—With the nation's basic steel industry shut down by a strike of 650,000 United Steelworkers members, the federal government made its first tentative move Sunday toward reviving contract negotiations.

Joseph F. Finnegan, director of the Federal Mediation Service, said in Washington he has

No Survivors Found; Attempt To Recover Bodies From Gorge Will Be Made Today

By LAWRENCE MALKIN

GRAND CANYON, July 1 (P)—Two huge airliners, turned into hurtling coffins for all 128 persons aboard presumably by colliding in flight, were found burned and shattered Sunday on adjacent peaks in Arizona's Grand Canyon.

No survivors could be found by a helicopter crew which battled turbulent air currents to land beside the wreckage on separate rock spires less than a mile apart in the desolate gorge.

The helicopter crew reported most of the bodies burned and mutilated beyond recognition.

As a single tragedy it was the worst commercial air disaster in history. Civil and military authorities gathered Sunday night to begin an investigation into the cause of the tragedy.

The helicopter first reached the wreckage of a Trans World Air Lines Super Constellation which carried 70 persons. Later it reached the United Air Lines DC7 less than a mile away. It carried 58 persons.

Figure 1.3. An Arizona Daily Star headline from July 2nd, 1956 that reported on the deadly Grand Canyon crash between Trans World and United commercial airliners [4].

During this time, the FAA began to define different classes of airspace based on factors like altitude and operational requirements [3] and published the first Federal Aviation Regulations (FAR, Title 14 of the Code of Federal Regulations). The FAA also oversaw the application of technological advances spurred by World War II to air traffic safety. Two-way center controller/pilot communications became commonplace, and radar was used to survey airspace surrounding airports and to dynamically track aircraft movements [4]. Soon, computers were also adapted for use in ATC centers, allowing electronic procedures to accomplish tasks that had previously been performed manually by controllers [4]. These technologies quickly became the foundation of the FAA's ground-based ATC system, which focused on managing traffic to maintain a minimum separation threshold between aircraft.

Figure 1.4. In the 1970s, air traffic control towers were equipped with computers, enabling automation of various tasks and increasing the capacity of the air traffic control system. This photograph shows air traffic controllers working in a modernized ATC facility [6].

In addition to benefitting the efforts of air traffic controllers to maintain adequate flight-separation, transponder, radar, and computing technologies accelerated the development of in-flight collision avoidance systems. Throughout the 1960s, industry studies investigated how these technologies could be used to create an onboard system for detecting, tracking, and evaluating collision threats. By the 1970s, manufacturers began to develop these systems [7].

Radar-based on-board collision avoidance equipment provided range, range-rate, and relative altitude information for both ‘cooperative’ and ‘non-cooperative’ aircraft, depending on the equipment used. These systems generated warnings to the pilot when the ratio of range over range-rate, also called Tau (τ), fell below a predetermined threshold [8].

The two main sensors used in early on-board collision avoidance systems were primary surveillance radars (PSRs) and secondary surveillance radars (SSRs). PSRs emit high-frequency signals and detect reflections from the target to determine the target’s flight characteristics. SSRs, on the other hand, detect signals transmitted from the target aircraft in response to an interrogation signal (see Figure 1.5.). While SSRs provide more accurate information at longer ranges, they rely on the target aircraft being equipped with the appropriate transponder equipment, limiting functionality to detecting so-called ‘cooperative’ aircraft. PSRs, on the other hand, are capable of detecting ‘non-cooperative’ aircraft which are not equipped with functioning transponders [9, 10].

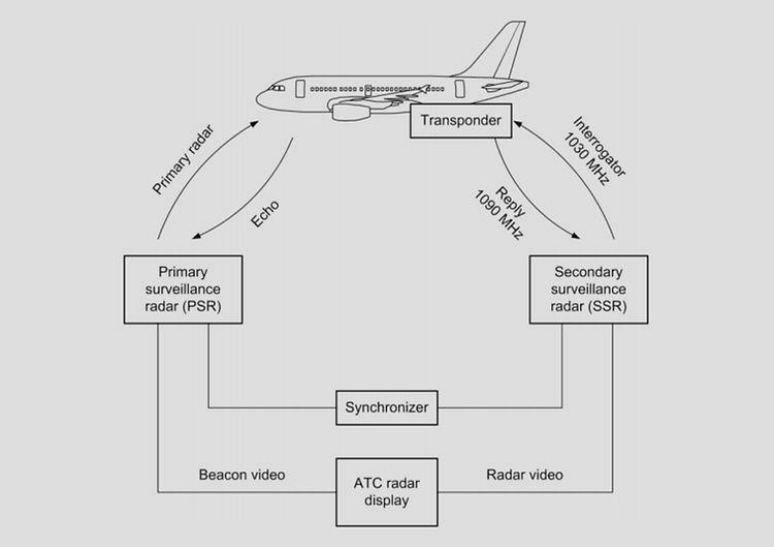

Figure 1.5. PSRs operate by sending a high intensity signal and sensing the low intensity echo or reflection from the target. SSRs operate by sending a low intensity interrogation and waiting for a response from an appropriately equipped, ‘cooperative’ aircraft [11].

Two decades of research into radar-based collision avoidance led to the development of a Traffic Alert and Collision Avoidance System (TCAS) [12]. TCAS-equipped aircraft interrogate SSR transponders of all nearby aircraft, providing real-time information about the position, altitude, and velocity of interrogated aircraft. This information is used along with a predefined separation threshold to determine whether nearby aircraft pose a collision risk. Aural and visual information can be provided to the pilot to assist with collision avoidance maneuvers when necessary [8]. TCAS continues to be a prominent traffic management and collision avoidance tool, along with new versions TCAS II and TCAS III.

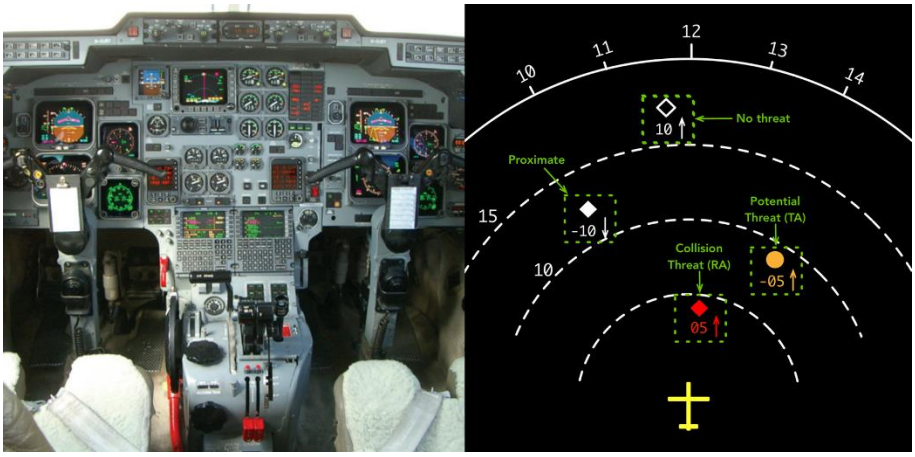

Figure 1.6. [Left] Aircraft cockpit equipped with TCAS II display and transponder. [Right] TCAS display close-up, with labeled symbols [13,14].

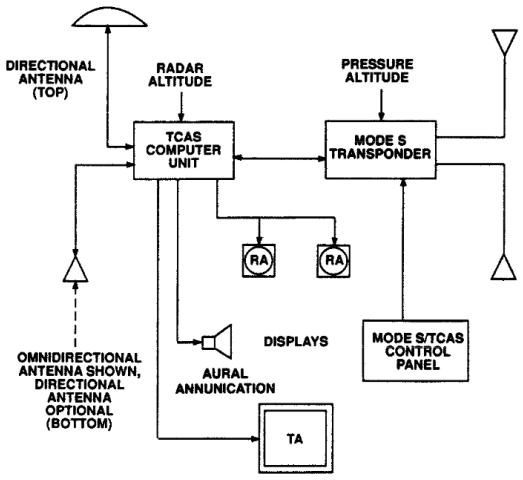

Figure 1.7. This TCAS II system diagram shows how azimuth and altitude information are directed through the TCAS computer unit to pilot display and aural signals [15].

Despite continued improvements to technology and modernization efforts, air traffic management and flight safety struggled under the burden of rising air traffic throughout the 1980s and early 1990s. In the mid-90s, the FAA began to transition the U.S. air system away from strict and detailed rules for air traffic operations to a 'free-flight' concept of flight rules. Free flight decreased the burden on air traffic controllers by allowing pilots to make use of new airspace awareness technology to make responsive decisions about flight operations [16].

Efforts to develop free flight-enabling technologies coincided with the launch of the U.S. Global Position System (GPS) in 1993. By 2001, the FAA and the Cargo Airline Association had developed the Automatic Dependent Surveillance-Broadcast (ADS-B) system, which uses on-board GPS sensors to send accurate position, speed, and identification data via satellite between planes and ADS-B ground receiving stations. ADS-B data can then be viewed by pilots and controllers. The advent of ADS-B dramatically improved airspace awareness capabilities, especially in regions which did not have radar coverage (like in Bethel, Alaska, where the FAA first officially implemented ADS-B technology) [16]. Table 1.1. shows a basic comparison between radar and ADS-B, as determined by a recent study by Andeme et al. (2021) which found ADS-B to be more accurate, efficient, and practical than radar-based airspace awareness. Figure 1.8. shows a block diagram of the ADS-B system.

Table 1.1. Basic comparison between Radar and ADS-B[a]

Radar	ADS-B
Aircraft location is transmitted every twelve seconds or more	Aircraft location is transmitted constantly (every second or more frequently)
Range limitation is found in some areas	The aircraft can be detected without restriction
Ground stations depend on human participation	Aircraft provide data without human participation
Expensive to buy, install, and maintain	Less expensive to buy, install, and maintain
Less efficient in search and rescue (MH-370, main case)	More efficient in search and rescue

[a]A more detailed parametric comparison of Radar and ADS-B can be found in source study [9].

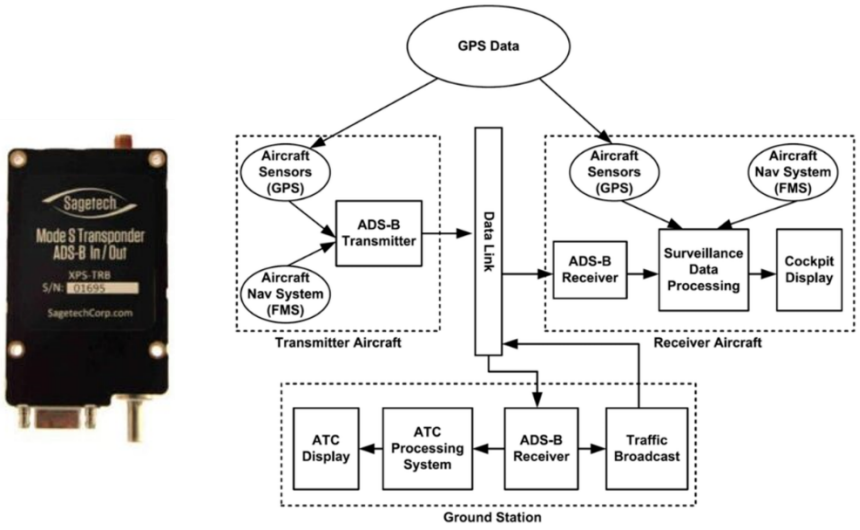

Figure 1.8. [Left] Picture of a Mode S Transponder with ADS-B In/Out capability. [Right] Diagram of the system architecture of ADS-B [17,18].

In 2003, the FAA announced the launch of their Next Generation Air Transportation System (NextGen). NextGen would comprise a broad range of modernization efforts, including:

- The transition from ground-based to satellite-based navigation.
- Automation and digital communication improvements.
- Continued movement toward precise but flexible flight routing.
- The development of collaborative decision-making capabilities.
- Integrated information management system development.
- Flight path and technology optimizations for environmental sustainability.
- Improved runway and airport operations to improve efficiency.

The FAA's NextGen initiative has been largely successful, as existing aircraft and air transportation system infrastructure has been updated to improve pilot and passenger safety [19].

In addition to the improvements mentioned above, NextGen has included preparations for the integration of increasing numbers of uncrewed aerial vehicles (UAV), also called uncrewed aerial systems (UAS) or remotely piloted aircraft (RPA), into the U.S. National Airspace (NAS). Similar to the aircraft collision avoidance efforts of the 20th century, recent preparations for UAV

integration have included the establishment of new regulations, research and development collaborations with industry and academic partners, and the implementation of a UAS Traffic Management (UTM) system. Section 1.2. provides a brief introduction to UAVs, exploring how the tools created for crewed air traffic control have been adopted and expanded to meet the growing need for autonomous collision avoidance capabilities.

1.2. Uncrewed Aerial Vehicles (UAVs) and Modern Collision Avoidance Efforts

Uncrewed aerial vehicles, colloquially known as drones, were invented during the mid-20th century for military use [20,21]. Following Hurricane Katrina in 2006, the FAA permitted the use of drones in civilian airspace to search for survivors of natural disasters, launching consequent research into civil, industrial, and consumer applications for UAVs [22]. Soon, select corporations were approved to use UAVs for pipeline inspections and agriculture [23], and companies like Parrot, DJI, and 3DR were experimenting with repurposing military UAV technology to suit a consumer market [22]. To ensure safety, early commercial UAVs were operated in segregated airspace or restricted areas, and collision avoidance was primarily achieved through manual piloting by ground-based observers.

As the commercial UAV market has grown, UAVs have garnered more attention for their potential to benefit civil and commercial applications in sectors like agriculture, infrastructure, filmmaking, emergency medical transport, environmental monitoring, and package delivery [24]. However, significant updates to UAV safety technologies are required to enable robust UAV operations for these applications. Moreover, UAV integration efforts need to address public concerns regarding the rising popularity of UAVs, including those regarding safety. Other concerns, such as privacy, environmental sustainability, and public stigma around the use of UAVs in military contexts, pose additional hurdles to broadening the application of UAVs [25].

By 2012, the FAA Modernization and Reform Act (FMRA) directed the FAA to develop a comprehensive plan for integrating UAVs into the NAS, enforcing a deadline for the development of a regulatory framework for small UAVs [26]. Then, in 2016, the FAA introduced Part 107 of Title 14 of the Code of Federal Regulations, establishing a framework for routine operations of small uncrewed aerial systems (sUAS) under 55 pounds. Commercial sUAS pilots were then required to demonstrate knowledge of aeronautics and airspace regulations, and they were prohibited from flying over people, beyond visual line of sight (BVLOS), and above specified altitude and speed limits [27].

Figure 1.9. FAA part 107 requires all commercial sUAS pilots (flying UAVs under 55 pounds) to acquire a remote pilot license, proving knowledge of aeronautics and airspace rules and regulations.

The same year that the FAA's Part 107 regulations prohibited BVLOS operations for commercial sUAS pilots, the UAS Traffic Management (UTM) concept was proposed by NASA [25]. UTM proposed a system of traffic management for low-altitude sUAS operations which combined airspace design, flight rules, operational procedures, ground-based systems, and UAV technical requirements. Following the proposal of UTM, NASA worked on developing Detect and Avoid (DAA) and Command and Control (C2) technologies, allowing UAVs to better sense nearby aircraft while maintaining a strong radio link with remote pilots [28,29]. These research and development efforts resulted in a series of successful test flights in 2020 and 2021. And in 2020, NASA's Aeronautics Research Mission Directorate initiated the Advanced Air Mobility (AAM) mission, which aims to engineer and demonstrate system level safety for aircraft of all sizes and altitudes of operation in the NAS [29].

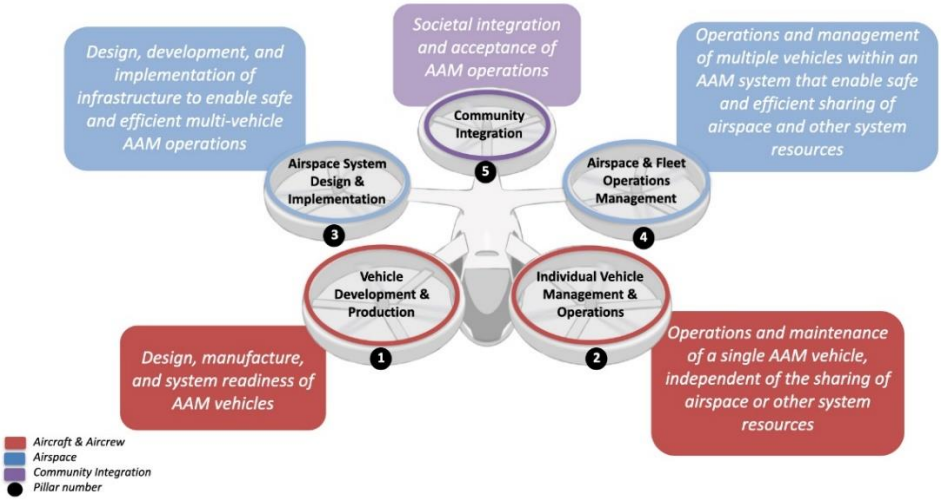

Figure 1.10. The guiding principles of NASA's Advanced Air Mobility (AAM) mission [30].

Of the many requirements for integrating UAVs into the NAS, DAA capability is among the most challenging and critical. Crewed aircraft have pilots to fulfill see-and-avoid responsibilities in the event of a collision course scenario (supported by cues from modern traffic awareness technologies like ADS-B and TCAS) [31-33]. For UAV operations in the pilot's line of site, see-and-avoid responsibilities can fall to the remote pilot. But for BVLOS operations, UAVs require an autonomous DAA system to determine the exact location of any nearby aircraft or obstacles, to evaluate the threat, and to direct collision avoidance maneuvers when necessary.

DAA-specific regulatory documents released throughout the 2000s have provided groundwork for specifying the necessary capabilities and technical requirements for DAA systems in various operational contexts [34-36]. For example, the ASTM's Document F2411-04el requires that DAA systems have FOVs of ±15° elevation and ±110° azimuth to maintain an equivalent level-of-safety to piloted see-and-avoid protocol. "Well clear" and "near mid-air collision" (NMAC) volume dimensions are also specified by regulatory documents based on standards for piloted aircraft. Testing the practical safety of these dimensions under different operating conditions for different UAVs has been a focus of recent DAA research efforts [37-40]. Figure 1.11. shows a

visualization of well-clear and NMAC boundaries provided in Loffi et al. (2022) which were applied to low-altitude test encounters between UAVs and general aviation (GA) aircraft.

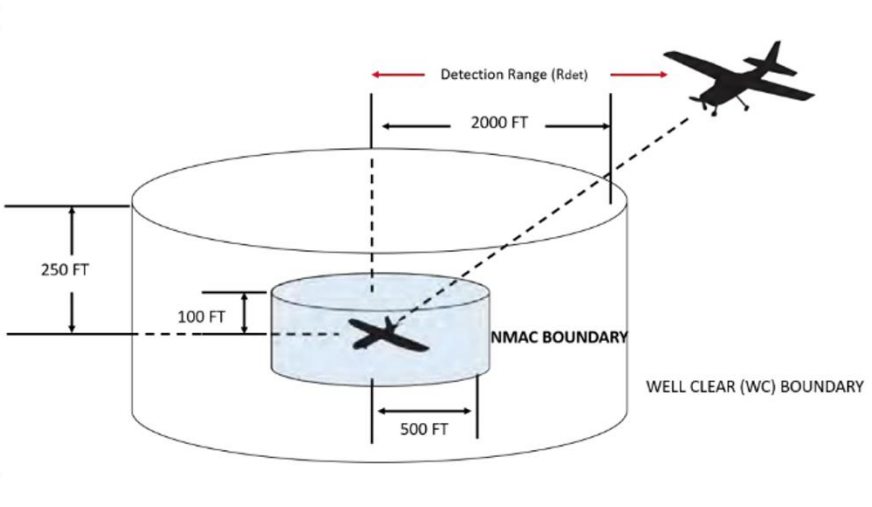

Figure 1.11. Example of well-clear and NMAC volume geometry. Well-clear and NMAC boundaries can vary depending on operation context and UAV characteristics like speed and size [41].

Significant progress has been made toward developing robust DAA capabilities for UAVs [42-44], but the fulfillment of NASA's vision for Advanced Air Mobility requires ongoing development efforts. Variability in size, speed, and operating altitude of UAVs gives rise to varying technical requirements for DAA systems. Different UAVs may be compatible with different sensors depending on SWaP (size, weight, and power) capacity, and depending on operation context, they may be required to detect both cooperative and non-cooperative air traffic [45]. Lastly, environmental factors like weather and illumination may affect the performance of some sensors more than others, meaning a successful DAA system often requires the fusion of multiple sensors.

While research and development efforts span a wide range of DAA system components, architectures, and concepts, all collision avoidance systems must accomplish a shared set of fundamental tasks: sensing the environment, conflict detection and awareness, selection of escape routes, and direction of collision avoidance maneuvers. In their literature review on DAA technologies for UAVs, Hottman et al. (2009) provide an overview of the requirements for each of these functions, as reproduced in Table 1.2.

Table 1.2. Requirements for DAA Systems[a]

Function No.	Function	Requirements
1.0	Detect conflicting traffic	• Continuously scan for threats • Minimize false alarms • Minimizes misses • Provides operator threat data • Covers a field of view of 110° horizontal and ± 15° azimuth[b] • Tracks all threats within a minimum range • Determines closure rates
2.0	Determine right of way	• Autonomously makes move in accordance with (IAW) FAA/International Civil Aviation Organization (ICAO) regulations • Operator makes move IAW FAA/ICAO regulations
3.0	Analyze flight paths	• Determines if target is heading toward danger zone (maintain 500-foot separation) • Calculate flight paths based on sensors available information • Updates time available for maneuver
4.0	Maneuver	• Maneuver IAW FAA guidelines • Allows operator maneuver • Maneuvers continuously in loss link/loss of command control (C^2) • Maintains at least 500-foot separation • Returns to original flight path after maneuver
5.0	Communicate	• Continuously reports to ground system; allows operator override • Available bandwidth exists to carry message packets • May use stand-alone telemetry or platform communications • Priority communication to maintain safety of flight • Reports targets when threat parameters are met; updates solutions until no longer a target

[a]From Hottman et al., 2009 [46].
[b]FOV specifications from ASTM Document F2411-04 [47].

Collision avoidance researchers Albaker and Rahim have broken these tasks into design categories, as reproduced below in Figure 1.12. This break-down of design factors helps

illustrate the breadth of engineering tasks required for the development of a successful DAA system.

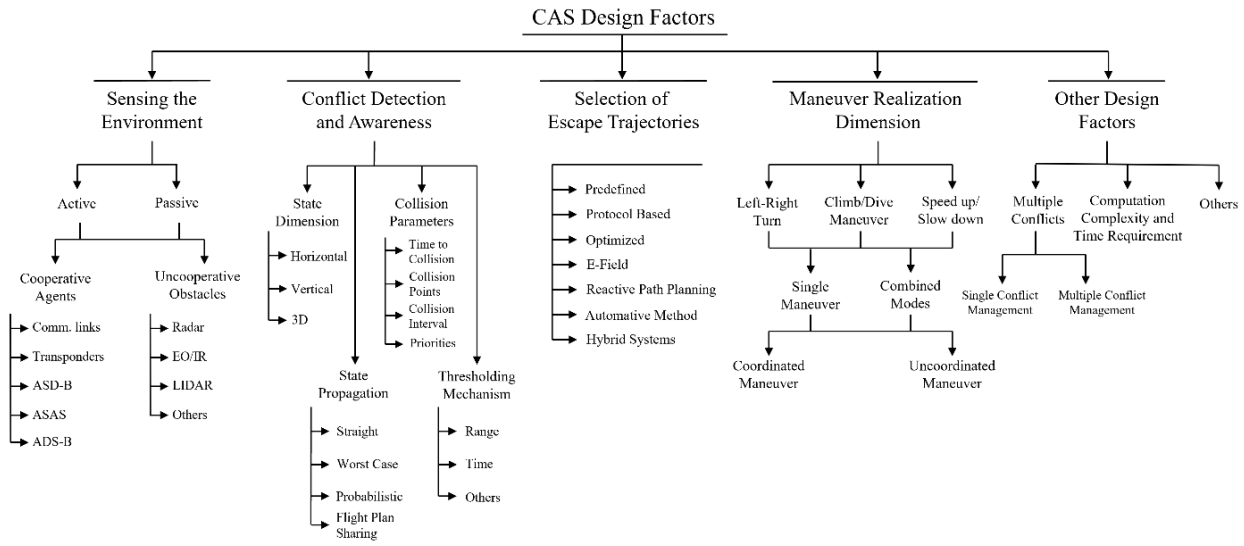

Figure 1.12. CAS, or collision avoidance system, design factors as summarized by Albaker and Rahim [45].

The challenge of designing diverse and adaptable DAA systems has given rise to a surge of research and development efforts. At the foundational level, researchers have worked to adapt DAA concepts to evolving UAV technologies and operational contexts [48,49]. Others have sought to distill precise technical requirements from regulations [50,51]. Similar work has defined and assessed measures for quantifying the success of collision avoidance systems [37,38,52] and has used quantitative analysis to model and simulate collision avoidance scenarios under a variety of conditions [39,40,53].

Algorithm development and testing has been another locus of work, including research on image processing, tracking algorithms, target classification, mapping, path prediction, and avoidance maneuver determination [54-59]. DAA algorithm development efforts have coincided with updates to collision avoidance algorithms for crewed aircraft traffic management; ACAS X (Airborne Collision Avoidance System X) has improved the deterministic collision avoidance logic of TCAS by introducing a probabilistic mode, including consideration for both crewed and

uncrewed aircraft (ACAS Xa and ACAS Xu) [12]. Another key development has been the application of machine learning techniques to detection tasks [60-62].

Researchers have also sought to define capabilities and requirements for a range of sensors [63-65]. As shown in Figure 1.11., transponder-based communications (TCAS), ADS-B, EO/IR (electro-optical and infrared sensors), radar, LiDAR, and acoustic sensors have been adapted to the task of UAV collision avoidance. These sensors can be divided into two categories: cooperative and noncooperative. As mentioned in the earlier discussion on PSRs and SSRs (see page 21), cooperative sensors require target aircraft to be equipped with the appropriate equipment. While these sensors are well-established and thoroughly tested, they are unable to sense uncooperative (i.e. unequipped) aircraft and ground-based obstacles like terrain features, towers, or power lines. Noncooperative sensors, like EO/IR, radar, and LiDAR, benefit from their ability to detect all types of objects (provided that the sensor in use is sufficiently sensitive to the signal of interest under operating conditions). Noncooperative sensors may be 'active,' meaning that they transmit a 'probe' signal and detect signal reflection from targets, or 'passive,' meaning they detect signals natively reflecting and/or emitting from targets. Most often, DAA systems employ sensors of multiple types (cooperative *and* noncooperative, active *and* passive) to ensure strong performance under a range of operational conditions [65-68].

Table 1.3. Overview of DAA sensor characteristics[a]

Sensor	Non-cooperative	Passive	Weather-Capable	Low-SWaP	Long Range	Low-Cost
TCAS	X	X	✓	✓	X	✓
ADS-B	X	X	✓	✓	✓	✓
Radar	✓	X	✓	X	✓	X
LiDAR	✓	X	✓	X	X	✓
Acoustic	✓	✓	✓	✓	✓	✓
EO	✓	✓	X	✓	X	✓
IR	✓	✓	X	✓	X	✓

[a]From Loffi et al. (2022) [41].

EO/IR sensors are becoming an increasingly popular non-cooperative sensor for DAA systems, especially on low- to mid-SWaP UAV platforms [63]. These sensors are lightweight, low-power,

and affordable, and they can provide high resolution imagery of surrounding airspace. However, they are unable to provide accurate range measurements, and system engineers must balance FOV and range performance requirements [64]. Experimental studies on the performance of commercially available EO/IR-based DAA systems typically assemble multi-camera systems using sensors from a single band, usually either visible (0.4 to 0.7 microns) or longwave infrared (8 to 14 microns), such that the cumulative multi-sensor FOV meets field of regard requirements (around 110º horizontal and ± 15º azimuth). EO/IR sensor range performance is then tested, with results varying depending on system resolution and field of view specifications [49,69].

Research on EO/IR design for DAA applications has yet to rigorously compare the sensitivity of detectors spanning the visible and infrared spectrum to aircraft under relevant atmospheric and illumination conditions. Such a band-performance comparison is necessary for fully understanding and optimizing EO/IR sensor design for UAV-based DAA systems, especially as detector technologies continue to advance across the visible and infrared spectrums. Chapter 3, titled "EO/IR Band Comparison of Aircraft-to-Sky Contrast and Range Simulations," shares results from a DAA-focused study of band performance for six EO/IR imagers in clear-sky, early morning, desert atmosphere conditions. This study measured the apparent contrast of the aircraft target (a C182 general aviation aircraft) at a close range, then using these measurements and relevant resolution and noise specifications to simulate detection range performance. This simulation demonstrates the effect of atmospheric degradation on apparent contrast over longer ranges, and results are shown for two atmospheres: desert and maritime.

Chapter 2, "Electro-optical and Infrared Systems," provides the technical background required to understand and critically engage with the contributions made in Chapter 3. Chapter 2 begins with an overview of the architecture of an EO/IR imaging system, covering illumination and source characteristics, atmospheric transmission, optics, detectors, and system electronics. After establishing a foundational understanding of EO/IR systems, I discuss common frameworks, metrics, and considerations for evaluating EO/IR system and band performance, focusing on those used to interpret study results in Chapter 3.

CHAPTER 2

Electro-Optical and Infrared (EO/IR) Systems

2.1. Introduction to EO/IR Systems

Electro-optical and infrared (EO/IR) sensors enable the detection and analysis of electromagnetic radiation spanning visible and infrared wavelengths. These sensors are used in a wide range of applications, including remote sensing, fire detection and monitoring, medical imaging, astronomy, environmental monitoring, and more. EO/IR sensors operate by detecting and converting the electromagnetic radiation emitted or reflected by objects into electrical signals. This conversion process relies on mechanisms which allow the intensity of visible and infrared radiation to be translated into digital information. Understanding the operational principles and capabilities of EO/IR sensors is foundational to optimizing their performance for a given DAA system. The following chapter provides an overview of EO/IR fundamentals from target characteristics to electronics, as these are the components most relevant to EO/IR design for automated DAA applications. Key components and associated quantitative parameters are summarized in Table 2.1., reproduced from Driggers et al., 2022.

Table 2.1. Sample of Analytical Parameters[a]

Illumination	Spectral Irradiance
Target	Reflectivity Emissivity Size and spatial characteristics Temperature
Atmosphere	Path radiance Obscurants Transmission Optical transfer function Scattering
Sensor optics	Lens transmissions Mirror reflectivity

	Filter transmission Aberrations Diffraction Aperture size and shape
Sensor detector	Responsivity Quantum efficiency Well capacity Detector angular subtense
Sensor electronics	Temporal characteristics Digital or analog filter characteristics
Display	Resolution Brightness and contrast
Human psychophysics	Temporal response Contrast threshold Brightness dependence
ATR or AiTR response	Discrimination probability False-alarm rate

[a]From from Driggers et al., 2022 [70].

2.1.a. Target and illumination characteristics

The operation of an EO/IR sensor begins in the scene of interest, where objects reflect and emit electromagnetic radiation across various wavelengths. Terrestrial remote sensing involves two main scenarios: in the first, ambient light (e.g., sunlight) illuminates the scene, where the illumination spectrum is modulated by interactions with objects that absorb and reflect light by wavelength. This scenario applies to reflective-band imagers like visible cameras (VIS, 0.4 to 0.7 microns), near-infrared cameras (NIR, 0.7 to 1 micron), short-wave infrared (SWIR, 1 to 1.7 microns), and extended short-wave infrared (eSWIR, 2 to 2.4 microns). In the second scenario, objects emit electromagnetic radiation due to thermal electron motion, which can be directly measured. This applies to emissive-band imagers like mid-wave infrared cameras (MWIR, 3 to 5 microns) and long-wave infrared cameras (LWIR, 8 to 14 microns) [70].

Planck's Law explains the spectral distribution of reflected and emitted radiation in terrestrial remote sensing:

$$M(\lambda, T) = \varepsilon(\lambda) \frac{c_1}{\lambda^5} \frac{1}{(e^{\frac{c_2}{\lambda T}} - 1)} \qquad [\text{W/cm}^2\text{- } \mu\text{m}]$$

where ε is the emissivity of the object, λ is wavelength in micrometers (μm), T is absolute temperature in degrees Kelvin, c_1 is 3.7418 x 10^4 Watts-μm^4/cm^2, and c_2 is 1.4388 x 10^4 μm-Kelvin. Planck's Law describes the spectral density of electromagnetic radiation emitted by a black body in thermal equilibrium at a given temperature. For terrestrial objects near 300 Kelvin, the law shows that black and graybodies emit peak radiation from 6 to 14 microns. For the sun at about 5500 Kelvin, peak emissions are in the visible spectrum, from 0.4 to 0.7 microns. Figure 2.1. shows two sets of blackbody emission curves: one for objects near solar surface temperatures, and one for objects near terrestrial temperatures. Wavelength bands corresponding to EO/IR imaging bands are highlighted.

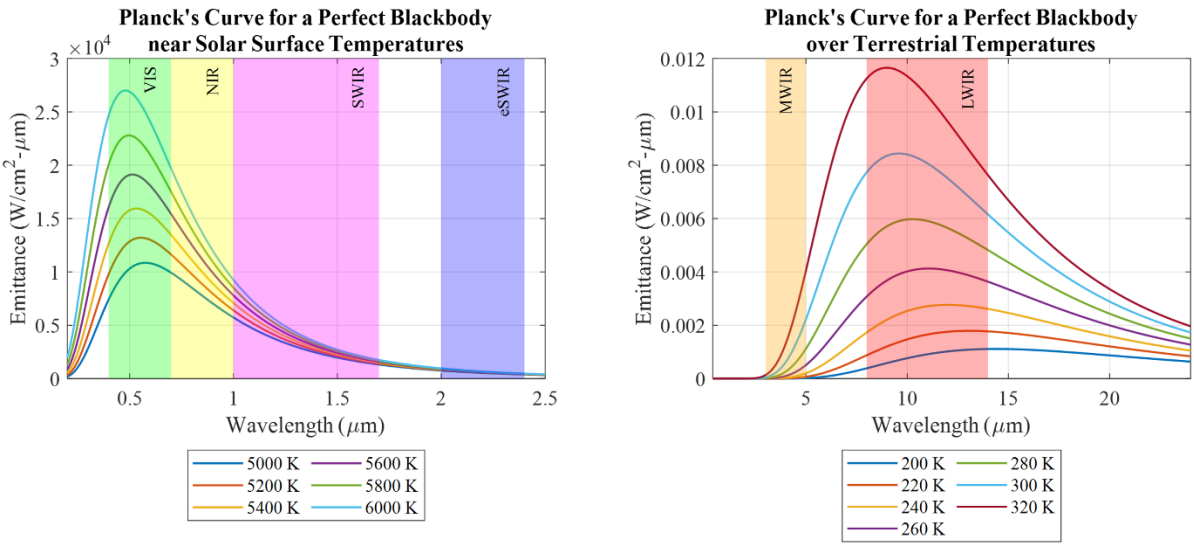

Figure 2.1. Planck's law describes the emittance spectrum of a source based on its temperature. The two curves shown represent blackbody emissions (emissivity of 1) for objects near-solar surface and near-terrestrial temperatures. Wavelength ranges corresponding to EO/IR imaging bands are highlighted.

During the day, solar radiation in visible and shorter infrared wavelengths (VIS, NIR, SWIR, and eSWIR, from 0.4 to 2.4 microns) illuminates terrestrial scenes. In longer infrared wavelengths (MWIR and LWIR, from 3 to 14 microns), signal is dominated by thermal emissions from the scene rather than reflected sunlight. It's important to note that not all objects emit radiation exactly as described by Planck's curve; their composition, structure, and surface properties affect electron movement and emission spectra. A perfect blackbody emits radiation as described by Planck's curve; a graybody emits similarly but with reduced magnitude; and a spectral emitter's emission varies by wavelength.

2.1.b. Atmospherics

As radiation emitted from or reflected by scene objects passes through the atmosphere, it encounters molecules, aerosols, and particulate matter, leading to absorption, scattering, and distortion. Absorption occurs when atmospheric particles absorb photons, attenuating specific wavelengths whose photon energies match the energy differences between the energetic states of the absorbing particle’s electrons. The absorption profiles of abundant atmospheric particles like carbon dioxide, hydrogen dioxide, and ozone disallow the transmission of certain wavelengths of light over long distances, as shown in Figure 2.3. Along with detector sensitivity, atmospheric transmission windows define the wavelength bands which are accessible to EO/IR sensors (see Figure 2.2.).

Different atmospheric conditions (foggy, smokey, hazy, etc.) correspond to increased density of particles, molecules, and particulate matter of different sizes, and consequently block different wavelengths of light. Generally speaking, longer wavelengths of light are better able to penetrate ‘dirty’ atmospheres than shorter wavelengths, making the reflective and emissive infrared bands useful for long-range imaging applications [70-72].

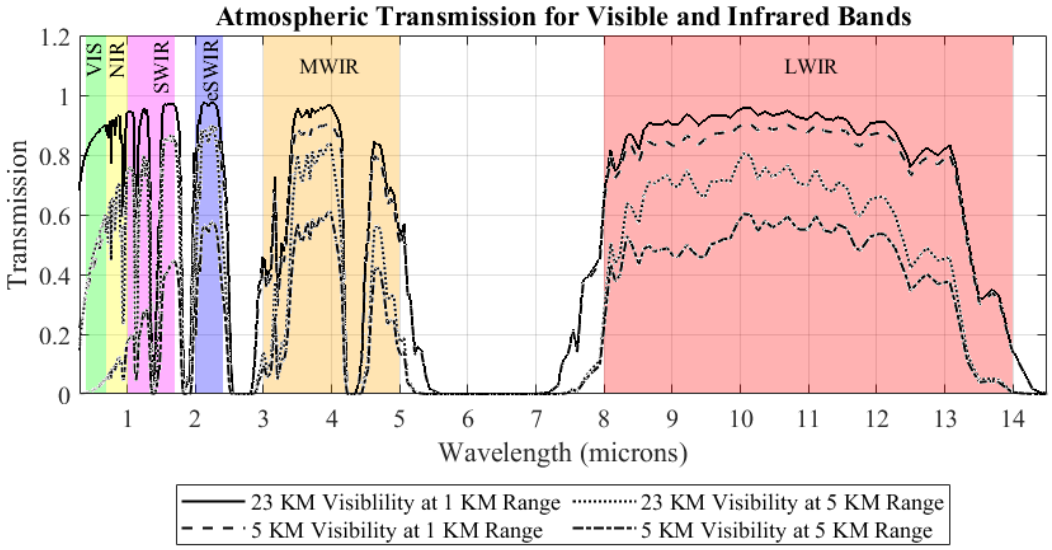

Figure 2.2. Atmospheric transmission as a function of wavelength, with EO/IR imaging bands highlighted. Four curves are shown, including two visibility conditions (23 KM and 5 KM) and two ranges (1 KM and 5 KM). Note that degraded visibility conditions and increases in range do not degrade transmission equally across all bands (compare VIS and eSWIR, for example). Data was pulled from MODTRAN.

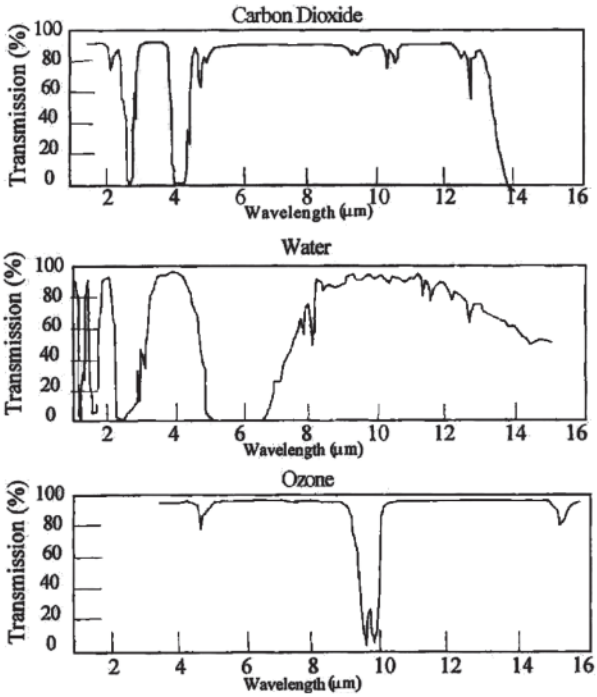

Figure 2.3. Transmission profiles for carbon dioxide, water, and ozone – three abundant atmospheric molecules. The absorption windows (low transmission) for these molecules align with the low transmission zones of the atmospheric transmission plot shown in Figure 2.2. [70].

Another important atmospheric phenomenon is scattering. Scattering diverts radiation from its original path, scattering it in various directions. There are three main scattering regimes: Rayleigh scattering, which is inversely proportional to the fourth power of the wavelength (meaning it is more prevalent at shorter wavelengths) and dominates when the particle radius is less than one-tenth the wavelength of the scattered light; Mie scattering, which occurs when the wavelength is about the same size as the particle; and scattering by particles much larger than the wavelength of incident light, which can be described by the geometrical optics model (see Figure 2.4.). Alongside blackbody emissions from atmospheric particles, scattering contributes to overall path radiance, increasing noise and reducing contrast between objects in the scene. Additionally, atmospheric turbulence due to fluctuations in temperature can create irregularities in refractive index, leading to effects like scintillation, further impeding the propagation of radiation through the atmosphere. These atmospheric interactions collectively contribute to the modification of radiation's intensity, spectral distribution, and polarization as it travels from scene objects to sensors.

Table 2.2. Common atmospheric particles and associated scattering regime[a]

Particle Type	Radius (μm)	Density (per cm^3)
Air molecules (Rayleigh)	10^{-4}	10^{19}
Haze particles (Rayleigh)	10^{-2} – 1	10 – 10^3
Fog droplet (Mie)	1 – 10	10 – 100
Raindrops (geometrical)	10^2 – 10^4	10^{-5} – 10^{-2}

[a]From Driggers et al., 2022 [70].

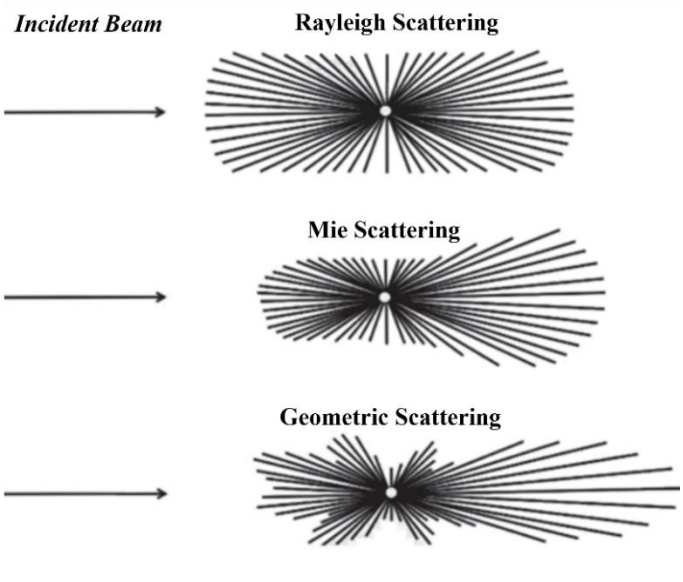

Figure 2.4. Illustration of scattering patterns for Rayleigh, Mie, and Geometrical scattering regimes. Rayleigh scatters evenly, Mie scatters 'forward,' and Geometrical scattering patterns can be described using geometrical optics principles [70].

2.1.c. Optics

After propagating from the scene to the sensor, reflected and emitted radiation are collected by sensor optics and focused onto the system detector array. Sensor optics are most often made of glass, and they may be paired with filters which selectively block unwanted wavelengths of light. Optical materials typically absorb and reflect a small portion of incident light, focusing, dispersing, or bending the rest as it transmits through the material. The amount of radiation which transmits through system optics can be described by an optical transmission constant.

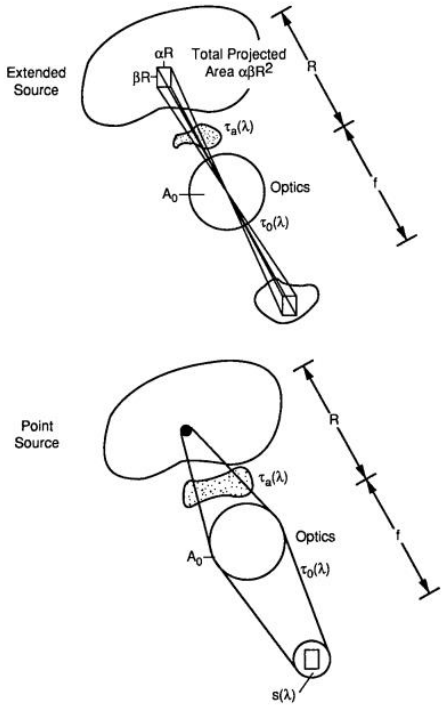

Figure 2.5. Optical energy collection by system optics [73].

Two models are most often used to describe the propagation of light through an optical system:

geometrical optics and physical optics. Geometrical optics models light as a bundle of rays that travel in straight lines, bending at interfaces between different media according to Snell's law and reflecting according to the law of reflection. This model is useful for designing lens systems where the wave nature of light can be neglected, allowing for simple calculations of image and object relationships, magnification, and system layout. Physical optics, on the other hand, models light as a wave, providing explanations for wave-like optical phenomena including diffraction, interference, and polarization.

While the tools of geometrical optics are usually sufficient for basic optical design, physical optics principles are required to understand how the design of an optical system will affect the resolution of the system. Consider the task of imaging a single, monochromatic point source through an optical system. When imaging a point source through an aberration-free optical system, the diffraction of light at the circular aperture of the system—typically the lens or a limiting diaphragm—results in a distinctive diffraction pattern at the image plane. The central bright spot, known as the Airy disk, is surrounded by concentric rings of diminishing intensity. The Airy disk represents the impulse response, or point spread function, of a diffraction limited optical system with a circular aperture. In other words, it is the best-focused spot that the system can produce. Figure 2.6. shows a graphical representation of this diffraction pattern.

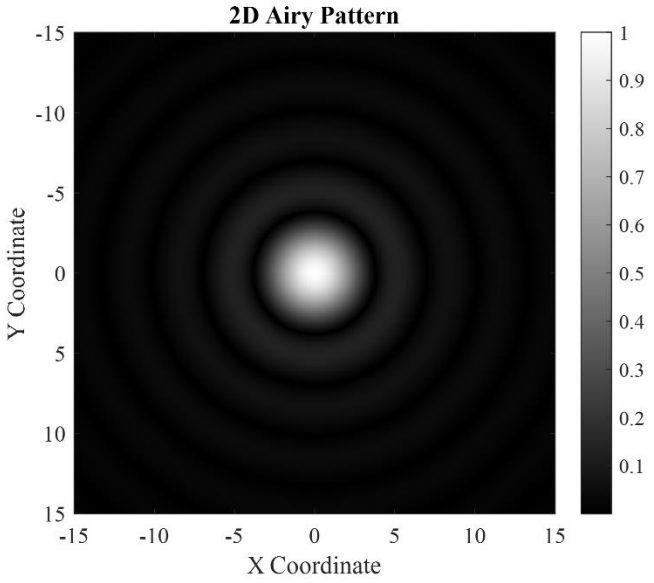

Figure 2.6. 2-D representation of an airy disk diffraction pattern, with its bright central region and concentric rings of decreasing intensity moving outward.

The intensity of the light *I* at an angle θ from the central peak of the Airy disk is given by:

$$I(\theta) = I_0 \left(\frac{2J_1(x)}{\mathrm{x}} \right)^2$$

where I_0 is the intensity at the center of the Airy disk, J_1 is the first-order Bessel function of the first kind, $x = \frac{\pi D}{\lambda} sin(\theta)$, D is the diameter of the system aperture, λ is the wavelength of light propagating through the system, and θ is the angle from the optical axis to the point of interest on the image plane. The argument (x) of the Bessel function links the physical properties of the system and the light source with the resulting diffraction pattern.

The radius of the central bright spot, or the first zero of the Airy function (where the intensity first drops to zero), can be used to define the size of the Airy disk. This radius (θ_{min}) on the image plane is given by:

$$\theta_{min} = 1.22 \frac{\lambda}{D}$$

The angular size of the Airy disk provides the fundamental limit to the resolving power of the optical system, often referred to as the diffraction limit.

To relate this angular measurement to a physical dimension on the image plane, on can multiply the angular radius by the effect focal length of the system, *f*. The diameter of the airy disk in the image plane, d_{Airy}, is:

$$d_{Airy} = 2 f \tan \theta_{min} \approx 2.44 f \frac{\lambda}{D}$$

with the approximation holding over small angles (small angle approximation: $\tan\theta \approx \theta$). These equations highlight the inverse relationship between the aperture diameter and the size of the Airy disk: a larger aperture results in a smaller Airy disk, leading to a higher resolution. Conversely, longer wavelengths of light lead to larger Airy disks, reducing the system's resolving power. This means that, for a diffraction-limited system, moving to longer wavelengths in the reflective bands allows increased range performance: this is because the increased spot size is insignificant relative to the reduced impact of scattering and absorption at longer wavelengths. In the emissive bands, on the other hand, there is a trend toward lower range performance at longer wavelengths due to an increasingly limited optical resolution [70].

2.1.d. Detectors, ROICs, and Sensitivity Metrics

Sensor optics focus electromagnetic radiation from the scene onto a detector array located at the optical image plane. The detector’s role is to take a continuous optical signal and convert it to a discrete array of electrical signals, which can then be transferred to a computer via readout integrated circuit (ROIC) and converted to a grid of gray or RGB values for image reconstruction. An EO/IR detector’s material characteristics, operating temperature, detector size, and pitch influence the overall system’s imaging band, sensitivity, and resolution. The conversion efficiency of optical to electrical signals is determined by the detector's ability to absorb photons, which requires the photon energy to exceed the material's bandgap.

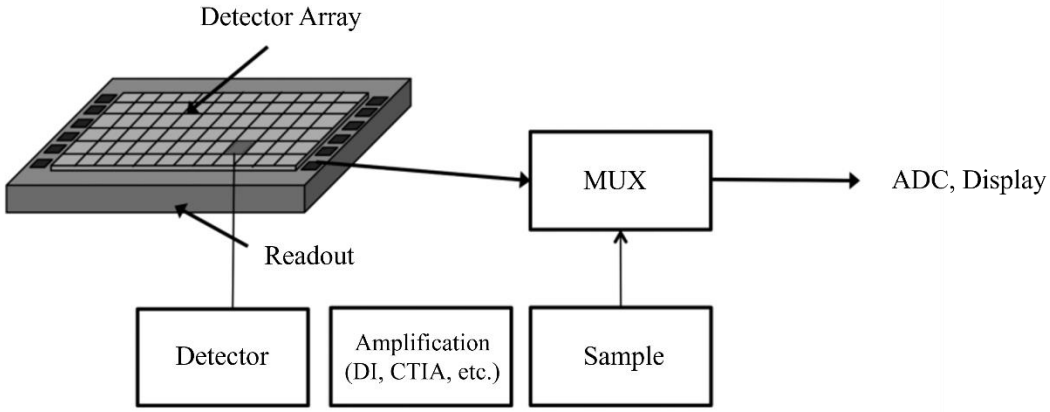

Figure 2.7. Schematic of a modern-day detector and ROIC. After the detector converts incident radiation into an electrical signal, unit cells detect, amplify, and sample the electrical signals. The ROIC then multiplexes signals from all unit cells and passes the signal to a computer for digitization and display. Schematic pulled from Driggers et al., 2022 [70].

EO/IR detectors fall into two categories: photon (quantum) detectors and thermal detectors. Photon detectors operate by converting absorbed photon energy into electrical signals, and can be further categorized into photoconductors, photovoltaics, and photo-emissive detectors based on their conversion mechanisms. Photoconductors detect light by varying the material's conductivity in response to light absorption. Photovoltaics generate a voltage from electron-hole pairs created at a P-N junction by absorbed photons. Photo-emissive detectors emit electrons from materials when photons are absorbed, a process requiring a vacuum environment for the electron transfer. Material choice is crucial, as it determines the bandgap and, consequently, the detector's spectral sensitivity and operating temperature. For instance, materials with wider bandgaps can operate at higher temperatures and are sensitive to shorter wavelengths, whereas materials with narrower bandgaps are suited for longer wavelengths but may require cooling to reduce noise [70].

Thermal detectors, including bolometers and pyroelectric detectors, convert absorbed radiation into temperature changes, subsequently measured as changes in electrical properties. Bolometers work by detecting resistance changes in a material due to temperature fluctuations, requiring materials with a high temperature coefficient of resistance for sensitivity. Pyroelectric detectors

measure changes in polarization due to temperature variations, with materials selected for their pyroelectric coefficient. Both types have improved significantly, offering faster response times and greater sensitivity without the need for cryogenic cooling [70].

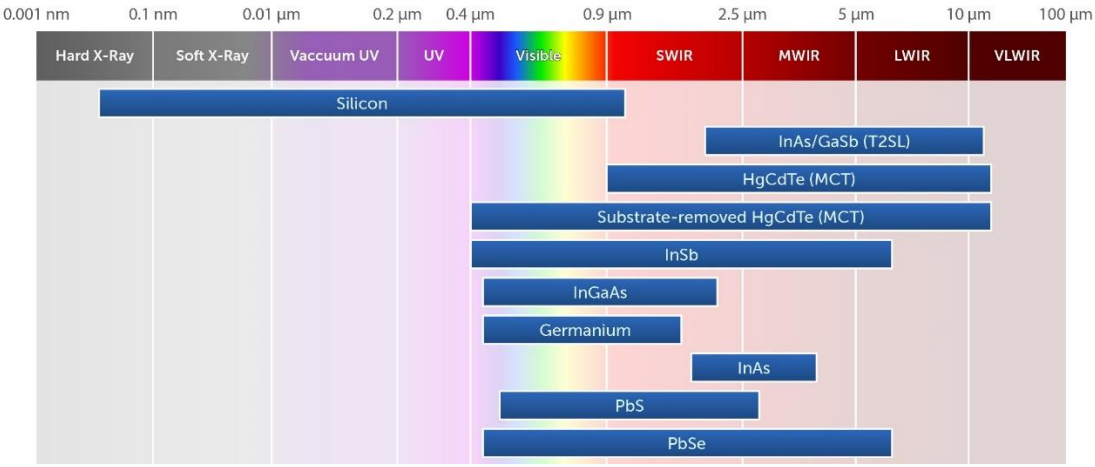

Figure 2.8. The sensitivity of a detector to a given wavelength of radiation depends on material characteristics of the detector. This figure shows a range of common detector materials and their general range of spectral sensitivities [74].

Detector performance can be quantified by several key metrics, including quantum efficiency, responsivity, and sensitivity. Quantum efficiency refers to the ability of a detector to convert incoming photons into electrons. This efficiency is expressed as a percentage, describing the proportion of photons successfully converted:

$$QE = T\ x\ FF\ x\ IQE\ x\ CE = \frac{\#\ electron\ (holes)\ collected\ as\ I_p/sec}{\#\ of\ incident\ photons/sec} \quad [\%]$$

where T represents the proportion of photons transmitted through the detector's antireflection coating and substrate, FF represents the detector's fill factor, IQE represents the internal quantum efficiency of the detector (the probability of photon absorption and electron generation), and CE represents the success rate of the ROIC (readout integrated circuit) moving electrons to be counted in the output. Losses at any stage can reduce QE, add noise to the system, and limit detector performance.

Responsivity, sensitivity, and normalized detectivity provide additional descriptions of a detector's conversion of optical signals to electrical ones. Responsivity describes the electrical output (in Volts or Amps) of a detector that results from a given optical input (in Watts or Lumens). Sensitivity, or signal-to-noise ratio (SNR), combines responsivity with an assessment of the noise level of the system, providing an assessment of whether a given optical signal can be differentiated from noise. For a resolved target, this is given by:

$$\frac{\Phi}{NEP} = SNR = \frac{\pi D^2 d_{det}}{8f^2\sqrt{\Delta f}} \int_{\lambda_1}^{\lambda_2} \varepsilon(\lambda) M(T,\lambda) D^*(\lambda)\, d\lambda \quad \text{[Unitless]}$$

where Φ is incident flux in Watts, D is the diameter of the system's entrance pupil, d_{det} is the diameter of the detector, Δf is the spectral bandwidth of the system, $\varepsilon(\lambda)$ is target emissivity, $M(T,\lambda)$ is target emittance, and $D^*(\lambda)$ is the detectivity of the detector ("dee-star"). This equation shows that, when detecting a resolved target, detector sensitivity is improved by increasing the F# of the system and increasing the detector size.

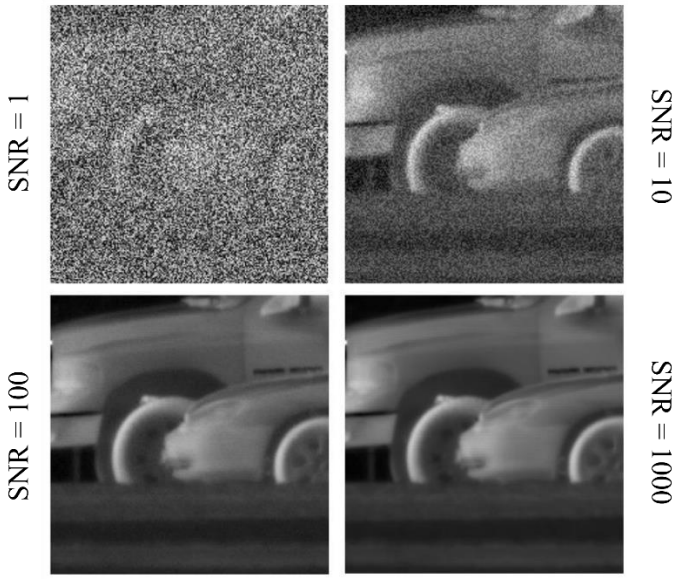

Figure 2.9. Comparison of various SNR values applied to a single image [70].

*D**, pronounced dee-star, normalizes SNR over the area of the detector and spectral bandwidth, providing an easily compared measure of a detector's ability to sense a weak signal in the presence of noise:

$$D^*(\lambda, f) = \frac{\sqrt{A_d \Delta f}}{NEP} \quad [\text{cm-Hz}^{1/2}/\text{Watt}]$$

D^* serves as a comprehensive measure that encapsulates the effects of quantum efficiency, responsivity, and overall sensitivity of photodetectors. While the basic definitions of responsivity, sensitivity, and detectivity apply to both photon and thermal detectors, the underlying mechanisms influencing these parameters differ, and different terminology is used in each context. For instance, thermal imagers refer to Noise Equivalent Temperature Difference (NETD) rather than Noise Equivalent Power (NEP).

Various noise sources impact the quality of the signal being measured by a detector: 1/f noise, photon noise, shot noise, Johnson noise, and readout noise. 1/f noise, also known as flicker noise, increases at lower frequencies and is prominent in semiconductor devices, affecting the stability and precision of low-frequency signals. Photon noise arises from the statistical nature of photon arrival times, setting a fundamental limit to detection sensitivity when the system is optimized to minimize other noise sources (often called BLIP, or background limited infrared photodetection). Shot noise is a type of quantum noise associated with the discrete nature of electrons flowing through a conductor, observable in most electronic devices, and is proportional to the square root of the average current. Johnson noise (thermal noise) is generated by the thermal agitation of electrons in a conductor and is dependent on the conductor's temperature and resistance. Readout noise refers to the noise introduced by the electronics involved in reading the signal from a detector, such as a CCD or CMOS sensor, and can be significant in low-light or high-precision measurements. Each of these noise types plays a critical role in determining the overall performance and sensitivity of detection systems across a broad spectrum of applications.

2.2. Characterizing System Resolution: Linear Systems Description of EO/IR System

Linear systems theory provides a powerful framework for understanding and characterizing the performance of electro-optical/infrared (EO/IR) systems, encompassing everything from target

illumination conditions to the electronics processing the detector's output. By treating EO/IR systems as linear, time-invariant (LTI) systems, one can analyze the combined effect of components on the overall system's ability to reproduce the scene being observed. Key concepts from linear systems theory used in this analysis include impulse response, modulation transfer functions (MTF), and the sampling theorem.

The impulse response of an EO/IR system describes how the system responds to a point source, characterizing the blur imparted by the system. This response is described using a point spread function (PSF). By determining the point spread function associated with the system, one can predict how the system will respond to more complex scenes, since the output image can be modeled as the convolution of the scene with the system's impulse response:

$$g(x) = f(x) * h(x) = \int_{-\infty}^{\infty} f(\alpha)h(x-\alpha)\,d\alpha$$

where g(x) is the output image, f(x) is the input, and h(x) is the point spread function.

The modulation transfer function, or MTF, provides a frequency domain representation of an EO/IR system's point spread function, showing how different spatial frequencies are attenuated by the system (look ahead to Figure 2.10 – the first image corresponds to a system whose MTF has a high cutoff frequency, and the second to a system with a lower cutoff). High spatial frequencies correspond to fine details in the scene, while low frequencies correspond to broader, more gradual changes. The MTF is derived from the Fourier transform of the impulse response and is a critical tool for assessing the resolution and detail that the system can capture:

$$H(\xi) = \mathcal{F}\{h(x)\} \; and \; h(x) = \mathcal{F}^{-1}\{H(\xi)\}$$

and

$$G(\xi) = F(\xi)H(\xi) = \int_{-\infty}^{\infty}\int_{-\infty}^{\infty} f(\alpha)h(x-\alpha)e^{-j2\pi x\xi}\,d\alpha\,dx$$

where $G(\xi)$ is the frequency spectrum of the output image, $F(\xi)$ is the frequency spectrum of the input, and $H(\xi)$ is the MTF. While component PSFs combine via convolution, component MTFs combine multiplicatively to form the system MTF:

$$PSF_{Sys}(x) = h_{Atmosphere}(x) * h_{Optics}(x) * h_{Detector}(x) * h_{Electronics}(x) * h_{Display}(x) * h_{Eye}(x)$$

$$MTF_{Sys}(\xi) = H_{Atmosphere}(\xi)\, H_{Optics}(\xi)\, H_{Detector}(\xi)\, H_{Electronics}(\xi)\, H_{Display}(\xi)\, H_{Eye}(\xi)$$

By analyzing an EO/IR system MTF, one can identify which components of the EO/IR system (e.g., atmospherics, optics, detectors) are limiting the system's ability to resolve detail and therefore focus on improvements where they are most needed.

Sampling theorem, also known as Nyquist-Shannon sampling theorem, provides tools for understanding the impact of digital detectors and electronics on an EO/IR system. It states that a continuous signal can be completely represented in discrete form and reconstructed without loss of information if it is sampled at a rate greater than twice its highest frequency component. This principle underlines the importance of the detector array's pixel density and the electronic sampling rate, ensuring that the system captures all the detail available in the scene without introducing aliasing artifacts.

While each of the above tools are pivotal for fully analyzing the resolution attainable by an EO/IR system, a full system analysis is not always necessary or expedient for quickly assessing the performance of a system. Oftentimes, it is helpful to compare the resolution of two components in particular: the system optics and detector array. This comparison has given rise to the $F\lambda/D$ metric, where F is the system f/# (focal length f over entrance pupil diameter D), λ is the wavelength of light propagating through the system, and 'D' is the detector pitch (d_{det}):

$$\frac{F\lambda}{d_{det}} = \frac{\lambda}{D}\frac{f}{d_{det}} = \frac{\sim Optical\ spot\ size}{Detector\ IFOV} = \frac{Sampling\ frequency}{Spatial\ bandwidth} \text{ [unitless]}$$

This metric quantifies the relationship between the diffraction-limited spot size created by the optical system and the spatial sampling interval provided by the detector array. A lower value of $F\lambda/D$ suggests that the system's resolution is more likely limited by the detector's sampling capabilities, whereas a higher value (>= 2) indicates that diffraction effects from the optics are the limiting factor. This comparison helps pinpoint whether the optics or the detector is the bottleneck in achieving higher resolution, guiding system designers in optimizing either component to enhance overall performance. By leveraging the $F\lambda/D$ metric, designers can achieve a balanced system where neither the optical design nor the detector unnecessarily

constrains the system's ability to resolve detail, even when a full system analysis is not feasible [75].

2.3. Combining Resolution and Sensitivity: CTF, TTP, and P(R)

When designing EO/IR systems, sensitivity and resolution metrics are both crucial for assessing overall performance. These metrics provide a comprehensive understanding of the system's capabilities, especially when characterizing the system's ability to perform specific tasks, such as target detection, recognition, and identification. The Contrast Threshold Function (CTF) and Targeting Task Performance (TTP) metric are two critical tools that integrate sensitivity and resolution measures to offer insights into the practical effectiveness of a given EO/IR system.

The Contrast Threshold Function (CTF) leverages both the sensitivity and resolution measures of an EO/IR system. CTF is a metric that quantifies the minimum contrast required for a given spatial frequency to be detectable. This function is directly influenced by the system's Modulation Transfer Function (MTF), as the MTF describes how different spatial frequencies are transferred by the system, indicating the system's resolution capabilities. At the same time, the system's sensitivity, including factors like detectivity (D*) and signal-to-noise ratio (SNR), affects the minimum detectable contrast. High sensitivity and a favorable MTF curve suggest a system that can discern low-contrast targets across a range of spatial frequencies. Figure 2.10. shows the interplay between resolution, contrast, and noise in determining the visibility of a range of spatial frequencies. Look ahead to Figure 2.11. to see a CTF plot.

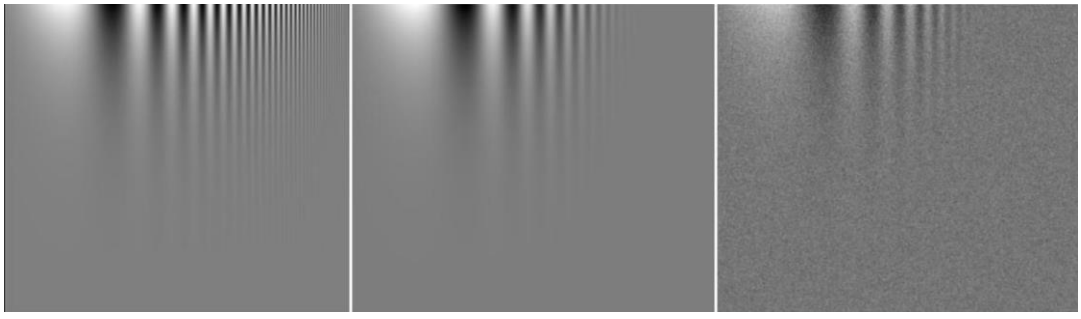

Figure 2.10. The three displayed images show how contrast, resolution, and noise impact the visibility of varying spatial frequencies. Each image shows increasing spatial frequencies from left to right and decreasing contrast from top to bottom. The left image shows a base image, the middle image is slightly blurred to reflect the impact of decreased resolution, and the right image shows the effect of noise. The regions of high visibility match the shape of the CTF curve (see Figure 2.11.) [70].

The system CTF is given by:

$$CTF_{sys}(\xi) = \frac{CTF(\xi)}{MTF(\xi)}\left(1 + \frac{\alpha^2\sigma^2(\xi)}{{S_{tmp}}^2}\right)^{1/2} \text{ [unitless]}$$

where $CTF(\xi)$ is the measured contrast threshold of the naked eye, $MTF(\xi)$ is the system Modulation Transfer Function, α is a calibration constant with units root-Hertz, $\sigma(\xi)$ is the noise filtered by the display and visual system (K), and S_{tmp} is the scene temperature that results in average display luminance.

The Targeting Task Performance (TTP) metric goes a step further by incorporating the CTF with models of human visual performance and task-specific details to predict how well an operator can perform a given targeting task using the EO/IR system. The TTP considers the visual acuity of the observer and the specific characteristics of the target (size, shape, and expected contrast) to determine how effectively the EO/IR system can be used to detect, recognize, or identify targets under various conditions. This metric effectively bridges the gap between the technical performance of the EO/IR system (as described by MTF and sensitivity measures) and the practical operational capabilities of the system when deployed in real-world scenarios. The TTP function can be expressed as follows:

$$TTP = \int_0^{\xi_{cut}} \sqrt{\frac{C_{tgt}}{CTF_{sys}(\xi)}}\, d\xi \quad \text{[cycles/mrad]}$$

where C_{tgt} is the apparent target contrast after atmospheric transmission and ξ_{cut} is the frequency at which apparent target contrast equals $CTF_{sys}(\xi)$. The calculated TTP value can be used to determine how many cycles on target are necessary for a given detection or identification task:

$$V(R) = \frac{L_{tgt}}{R} TTP \qquad \text{[cycles on target]}$$

where V(R) is the number of effective cycles on target for the given L_{tgt} (target characteristic dimension, which is the square root of target surface area), R (range to target), and TTP (based on apparent contrast, system resolution, and sensitivity). V(R) can then be used to predict the probability of success (at detection, identification, etc.):

$$P(R) = \left(\frac{V(R)}{V_{50}}\right)^{1.5} \Big/ \left(1 + \frac{V(R)}{V_{50}}\right)^{1.5} \qquad \text{[unitless]}$$

where P(R) is the probability of success as a function of range, V(R) is the number of effective cycles on target, and V_{50} is the task difficulty parameter (for example, this parameter is typically set to 2 for a detection task). Figure 2.11. shows the workflow for using the CTF, TTP, V(R), and P(R) to estimate range performance for a given task. The Night Vision Integrated Performance Model (NVIPM) provides a suite of tools for analyzing EO/IR system performance using sensitivity, resolution, and noise specifications alongside the TTP to estimate probability of detection at-range.

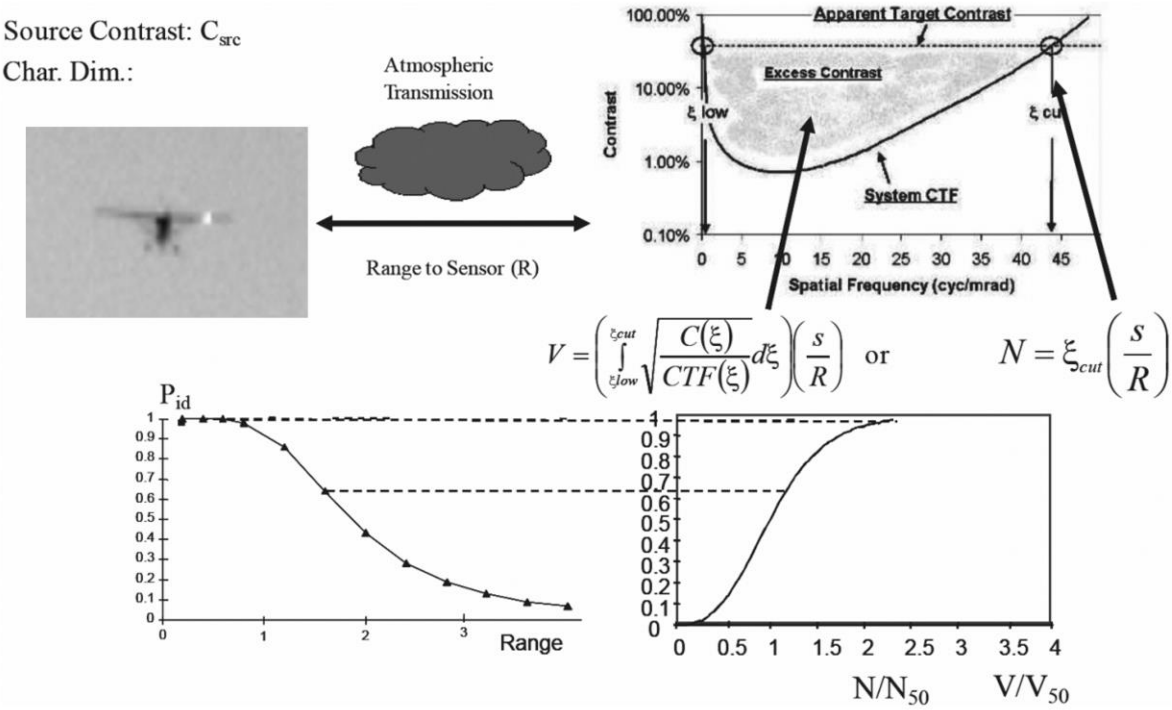

Figure 2.11. Measurements of apparent contrast can be used alongside system resolution and noise specifications to estimate range performance using the system CTF, the TTP metric, and the required number of effective cycles on target for a given detection or identification task [70].

2.4. EO/IR Sensing for Collision Avoidance

The above summary of EO/IR system components and design considerations provides a foundation for thinking through the design of an EO/IR system for DAA applications. As mentioned in Chapter 1.2., prior studies have tended to focus on analyzing tradeoffs between FOV and range performance in the visible and long-wave infrared bands, varying corresponding optical design parameters (see pages 32 to 33). While these are certainly important considerations, EO/IR design also requires understanding target characteristics (e.g., size, reflectivity, and emissivity) and the illumination and atmospheric conditions under which the UAV may operate. This includes considering how variability in daylight under different weather and climate conditions, dusk and dawn, and night operations may affect the visibility and contrast of potential obstacles or other UAVs. The effect of such variations in illumination and

atmospheric conditions will be more severe in some imaging bands than others, and, for daytime imaging in reflective bands, they will vary also with illumination angle.

Chapter 3 shares results from an introductory study of aircraft-to-sky contrast and detection range performance in the visible (VIS: 0.4 to 0.7 μm), short-wave infrared (SWIR: 1 to 1.7 μm), mid-wave infrared (MWIR: 3 to 5 μm), and long-wave infrared (LWIR: 8 to 14 μm) bands. This study examines variations aircraft-to-sky contrast over 8 illumination angles corresponding to the cardinal and ordinal directions under morning, clear sky conditions. A C182 general aviation aircraft was used for the data collection, as this aircraft is characteristic of a likely collision risk target. Contrast in the two reflective bands (VIS and SWIR) is determined in terms of equivalent reflectivity, and contrast in the two emissive bands (MWIR and LWIR) is determined in terms of equivalent blackbody temperature. The experimental sensitivity data is then used alongside resolution specifications to estimate detection performance at-range using the Night Vision Integrated Performance Model (NVIPM). Results are extrapolated to a maritime atmosphere using the MODerate resolution atmospheric TRANsmission model (MODTRAN). Analysis of contrast, range-performance, and recommendations on band selection are provided for reference in the design of EO/IR systems for aircraft collision avoidance. Future research may study band performance at night and against other backgrounds (e.g. clouds, ocean, ground terrain); under different atmospheric conditions; over a range of elevation angles with respect to the horizon (above, at, and below); and using varied approaches to the optical design of the experimental testbed.

Figure 2.12. Imagery of C-182 type general aviation aircraft at a range of 1000 m (left to right: high-resolution VIS, SWIR, MWIR, and LWIR).

CHAPTER 3

EO/IR Band Comparison of Aircraft- Sky Contrast & Range Performance Simulations

3.1. Sensors

The sensors used in this study included three VIS cameras with varying detector resolutions, a SWIR camera, a MWIR camera, and a LWIR camera. Off the shelf lenses were selected to match the cameras' horizonal fields of view to approximately 25 degrees. It is worth emphasizing that most previous studies on EO/IR performance for DAA systems have used sensors with larger FOVs (between 40 and 100 degrees). These studies test EO/IR performance for a DAA system architecture which uses EO/IR sensors as a wide-FOV element to fulfill DAA field-of-regard requirements (for example, ASTM Document F2411-04 requires DAA systems to have a $\pm 110^{\circ}$ azimuthal field of view). As part of a joint research effort with SARA to develop their Acoustically-Cued Electro-Optic (ACE-O) DAA system, this study assumed that acoustic sensors would fulfill the system's field of regard requirement. The acoustic sensor modeled as the initial detection instrument was SARA's Passive Acoustic Non-cooperative Collision-Alert System (PANCAS), which has a 360° field of regard, 100% accuracy (no false-detections), a 5-to-10-kilometer initial detection range, and an approximately 20-degree error cone [76]. The EO/IR system was designed to have its horizontal field of view (HFOV) cover the 20-degree error cone of PANCAS with some margin for error, serving as a secondary detection mechanism which determines the bearing of the target before cueing a laser range finder to determine the range to target.

Matching sensor HFOVs to $25\text{-}30^{\circ}$ led to some variations in the IFOVs among the testbed sensors. While varying IFOV may significantly affect contrast measurements for poorly resolved targets, using imagery of a close-range, highly resolved target for contrast measurements minimized the effect of varying detector resolution. Special care was taken to avoid unresolved

pixels during contrast analysis. This approach to analysis ensured that study results are relevant to diverse DAA architectures, regardless of their EO/IR FOV requirements.

The VIS cameras were monochromatic Allied Vision Alvium (AVA) CMOS sensors. The AVA 1800 U-240m had a 1936 by 1216 detector format and 3.45 μm pitch; the AVA 1800 U-507m had a 2464 by 2056 format and 3.45 μm pitch; the AVA 1800 U-2040m had a 4512 by 4512 format and 2.74 μm pitch. The SWIR camera was also Allied Vision Alvium, with an InGaAs sensor, 1296 by 1032 format and 5 μm pitch. The MWIR camera was a Telops Spark M150, with a cryo-cooled InSb sensor, 640 by 512 format and 15 μm pitch. The LWIR camera was a FLIR T1020, with a VOx sensor, 1024 by 785 format and 17 μm pitch. The measurements in the paper are resolved measurements for all sensors, meaning that the target at-range was larger than the IFOV for each sensor. Additional specifications of the ground-based testbed sensors are given in Table 3.1. Quantum efficiency curves for each sensor are shown in Figure 3.1. Figure 3.2. shows the number of pixels on target as a function of range for each testbed sensor, with the target's characteristic dimension matching that of a Cessna 182 viewed from the front (matching the study aircraft). Below this plot is a picture of the sensors mounted on the ground-based testbed used for the study.

Table 3.1. Camera System Specifications

Camera	Sensor Type	Band	Format	Pitch (μm)	EFL (mm)	F#	IFOV (mrad)	HFOV (deg)
AVA 1800 U-240m	CMOS	VIS	1936 x 1216	3.45	12	4	0.288	31.9
AVA 1800 U-507m	CMOS	VIS	2464 x 2056	3.45	16	4	0.216	30.4
AVA 1800 U-2040m	CMOS	VIS	4512 x 4512	2.74	25	4	0.110	28.3
AVA 1800 U-130 VSWIR	InGaAs	SWIR	1296 x 1032	5	12	1.8	0.417	30.9
Telops Spark M150	InSb	MWIR	640 x 512	15	25	1.1	0.600	22.0
FLIR T1020	VOx	LWIR	1024 x 785	17	35	3	0.486	28.5

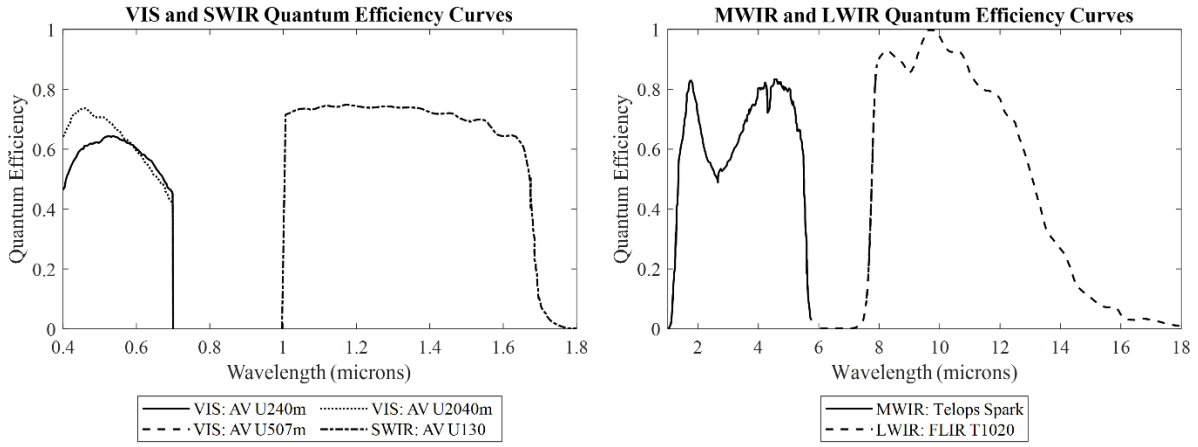

Figure 3.1. Quantum efficiency curves for testbed sensors. VIS and SWIR curves including low- and long -pass filters are shown on the left, and MWIR and LWIR curves are shown on the right.

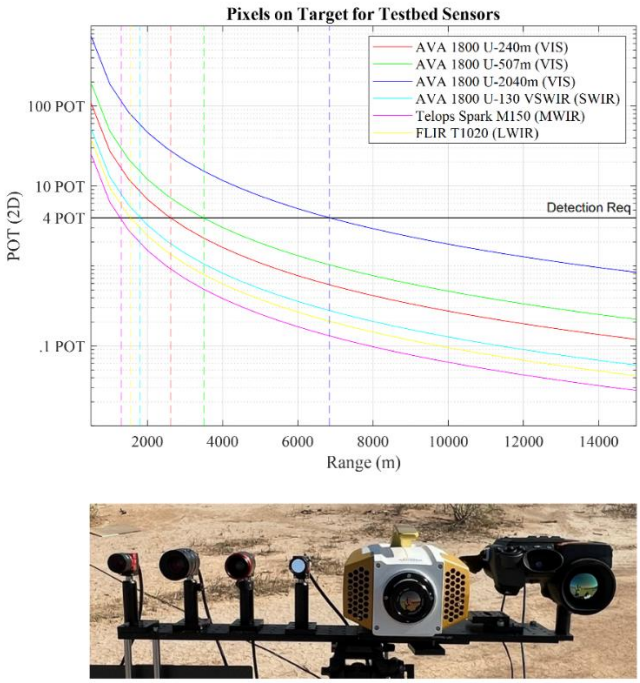

Figure 3.2. [Top] Pixels on target plotted as a function of range for all testbed sensors. This plot gives a comparison of detector-limited resolution given detector pitch and the chosen HFOV (25-30 degrees). [Bottom] Image of fully assembled testbed at study site. Sensors from left to right are as follows: low-resolution VIS, mid-resolution VIS, high-resolution VIS, SWIR, MWIR, and LWIR.

3.2. Calibration

The VIS and SWIR cameras were calibrated using a painted black and white target of known reflectivities illuminated by direct sunlight. Calibration images were taken immediately before the test flight to match sensor calibration to study illumination conditions. Calibration target image data was used to set the dynamic range of the cameras via adjustments to integration time. The black paint used was Krylon Industrial Ultra Flat Black Acryli-Quik spray paint; the white paint was Edmund Optics Pre-Mix White Reflectance Coating. Figure 3.3 shows the spectral reflectivity of these paints over reflective band wavelengths (0.4 to 2.4 μm). For SWIR, the average reflectivities for white and black paint were 0.947 and 0.029, respectively. For VIS, the average reflectivities for white and black were 0.977 and 0.021 [77,78].

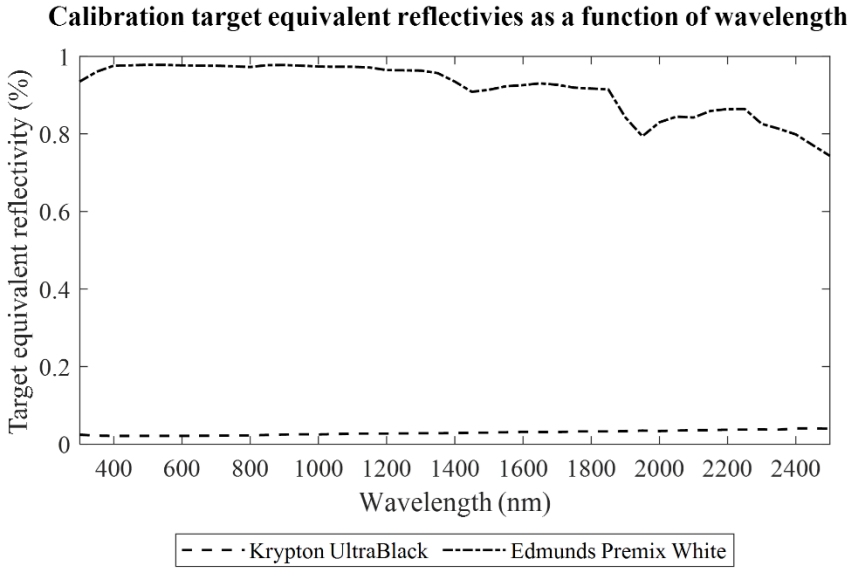

Figure 3.3. The spectral reflectivity values of the paints on the VIS/SWIR calibration target.

Calibration imagery in each band was used to relate image gray levels to equivalent reflectivity values for the given illumination conditions. Regions of interest within the black and white target regions were chosen for imagery captured by each sensor. Gray values were averaged over each region, and that value was associated with the corresponding equivalent spectral reflectivity. The two data pairs for the black and white regions were used to estimate a System Intensity Transfer

Function (SITF), allowing conversion from gray levels to equivalent reflectivity values during contrast data analysis. Figure 3.4. displays the SITF curves for the VIS and SWIR cameras under study illumination conditions.

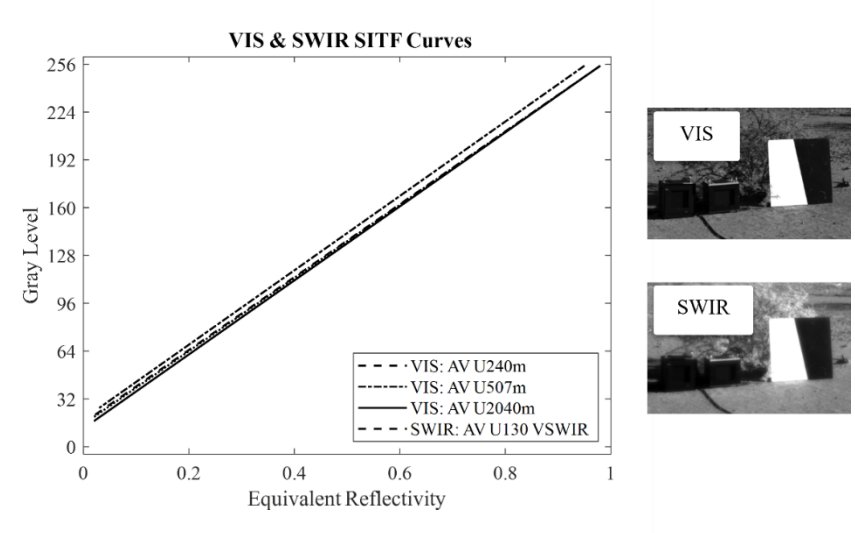

Figure 3.4. [Left] SITF Curves for the three VIS sensors and SWIR sensor and [Right] corresponding calibration imagery.

The MWIR and LWIR cameras were calibrated using blackbody sources at 20°C and 50°C. At these temperatures, the blackbody sources provided infrared radiation of a known emittance (W/m^2). The MWIR and LWIR sensors detected the radiant flux from each source over their respective wavelength bands, and the flux was converted to the corresponding gray level value. By associating the gray level values of the imaged blackbody sources with their known blackbody temperatures, we created SITF curves for the MWIR and LWIR sensors that mapped imagery gray values to their equivalent blackbody temperatures. The MWIR and LWIR SITF curves are displayed in Figure 3.5.

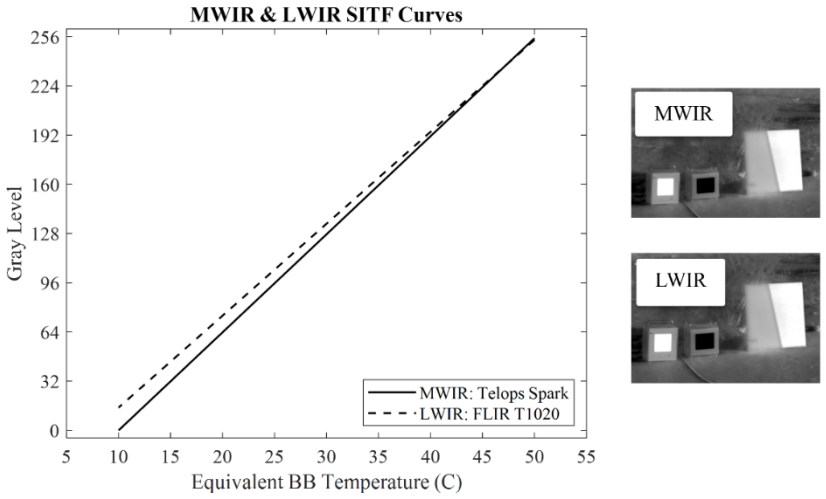

Figure 3.5. [Left] SITF curves for the MWIR and LWIR sensors and [Right] corresponding calibration imagery.

3.3. Data Collection

The initial aircraft-to-sky imagery data collection was performed in Northern Marana, Arizona on June 23rd, 2023 from 8:30 am to 9:15 am. The data collection objective was to collect simultaneous imagery of a Cessna 172 aircraft from eight vantages (corresponding to the cardinal and ordinal directions) using the six testbed sensors described in Table 1 and shown in Figure 3.2. The Cessna 172 was chosen as a representative crewed general-aviation aircraft. Imagery was captured continuously in all bands at four frames per second as the aircraft approached the testbed from ranges covering 3000 m to 500 m. For each approach, the sensor testbed was aimed at the appropriate region of sky and left untouched for the duration of the approach. The Cessna 172 pilot gradually descended (about 1000 feet per minute) over the course of the approach such that the aircraft remained near the center of the sensors' fields of view over the course of the flight. After each approach, the pilot immediately repositioned to approach at a range of 3000 m from the subsequent direction of approach. Between approaches, the testbed was reoriented to view the subsequent appropriate region of sky. Due to limited time between approaches (2 to 3 minutes), calibration imagery was taken once immediately before the initial aircraft approach and image collection. Throughout the flight, ADS-B data was recorded,

allowing correlation of study imagery with precise GPS locations on the aircraft. For figures showing the geometry of the flight path and ADS-B display, see Appendix A (Figures A.1. and A.2.).

This initial data collection did not yield a complete set of imagery for all sensors in all intended directions. Difficulties included coordinating a time-sensitive and complex flight/image capture plan; challenges with the reflective-band simultaneous capture software; severe glare in reflective band imagery facing into the sun; and obstructions to the testbed line-of-sight in some cardinal and ordinal directions. These difficulties informed modifications to the subsequent data collection plan. The subsequent collection involved more thorough collaboration with our pilot and the owners of the land used for the study site, updates to the simultaneous image capture software, use of a sunshade for sun-facing imagery, and the selection of a new test site with minimal line-of-site obstructions.

In addition to enabling the refinement of the data collection plan, the Marana data yielded some helpful qualitative and quantitative insights. Clear imagery of the aircraft's southbound approach from 2500 m to 500 m, included in Figure 3.6., suggested that SWIR would perform relatively poorly at detecting the plane against the sky due to low signal from the plane and low sky path radiance. LWIR performed poorly compared to MWIR. All VIS imagery displayed a bimodal aircraft signal (dark and bright spots relative to a gray background). The dependence of plane-to-sky contrast on illumination and other factors (time of day, aircraft color, etc.) in VIS imagery suggested potential difficulty for detection with fewer pixels on target. The GPS data collected alongside imagery from the Marana collection also allowed verification of the accuracy of a ground sample distance-based range estimation method of aircraft imagery with a range-to-target of 1000 m, which was the method used in the following study.

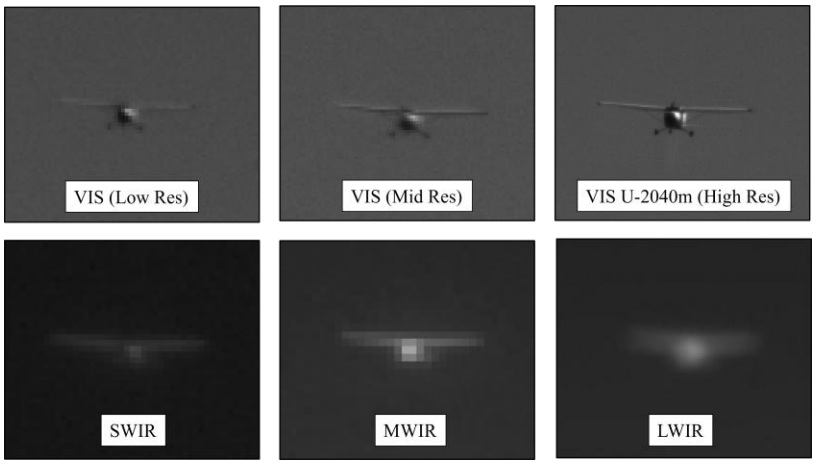

Figure 3.6. Labeled imagery of southbound Cessna 172 illuminated from the East, captured in initial data collection in Marana, AZ on June 23rd, 2024.

A second data collection was performed in Picture Rocks, Arizona on July 4th, 2023 from 7:45 am to 8:40 am. A summary of solar angles, visibility, and air quality at the time of the study is recorded in Table 2. The collection plan was similar to the prior data collection: the aircraft, this time a Cessna 182, approached the testbed from 8 directions, descending gradually to remain near the center of the sensors' fields of view. See Figure A.3. in Appendix A for a photograph of the study aircraft and schematics showing aircraft dimensions. Figure 3.7. shows a diagram of the test site, aircraft descent paths, and solar azimuth angle. For this study, imagery of the aircraft was collected from 5000 m to 500 m. The collection successfully recorded the aircraft against a clear sky background in the four bands of interest over the eight illumination conditions. Figure 3.8. shows imagery at 1000 m to target for the high-resolution VIS, SWIR, MWIR, and LWIR sensors over all aspect angles. Before the collection began, the sensors' exposure times were set to maximize their dynamic range based on calibration targets. VIS and SWIR calibration was based on a black-and-white target with known spectral reflectivity, and the MWIR and LWIR calibration was based on two blackbodies with equivalent blackbody temperatures of 20 degrees and 50 degrees Celsius.

Table 3.2. Summary of the date, time, atmospheric, and illumination conditions of Picture Rocks study[a]

Date and Time	Avg. Solar Azimuth	Avg. Solar Elevation	Visibility	PM 1 ($\mu g/m^3$)	PM 2.5 ($\mu g/m^3$)	PM 10 ($\mu g/m^3$)	R.H.
7.04.2023 7:45 to 8:40 am	82°	32°	10	13	16	4	18

[a]From Weather Underground [WU], the NOAA ESRL Solar Position Calculator [SP], and The World Air Quality Index Project.

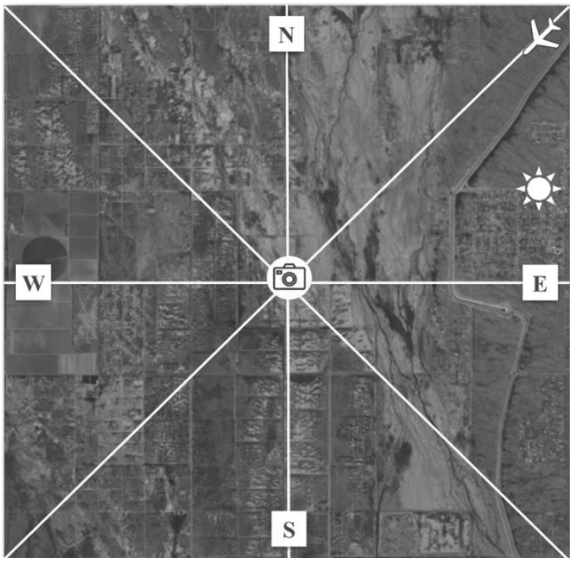

Figure 3.7. The second study site was located at 32.5803, -111.2091 in Picture Rocks, Arizona. The figure above shows the solar illumination angle (from the East), as well as the eight paths of approach taken by the Cessna 182. Each path of approach corresponded to a different illumination angle on the aircraft.

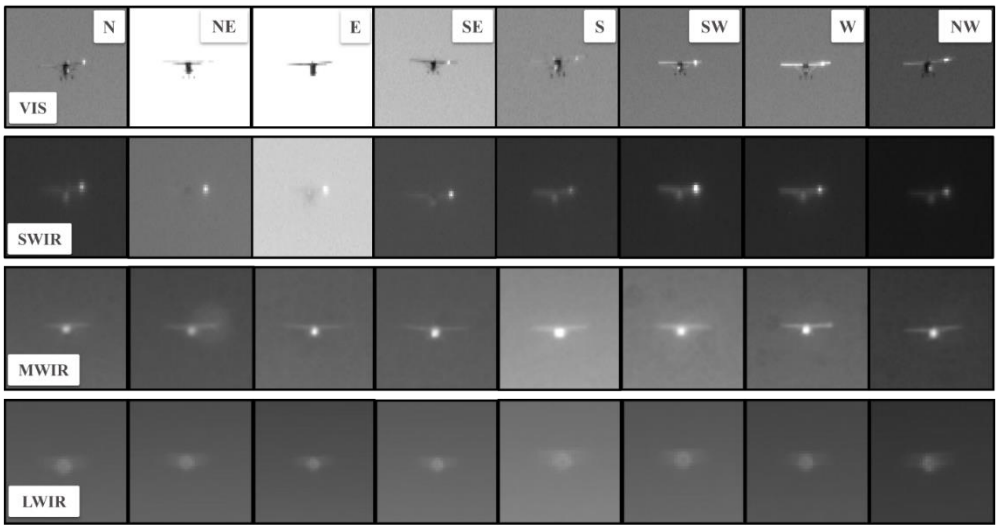

Figure 3.8. Aircraft imagery at a range of 1000 meters, including high resolution VIS, SWIR, MWIR, and LWIR for each aspect angle. Imagery shows a strong dependence on illumination angle for VIS imagery, some dependence for SWIR imagery, less still for MWIR imagery, and minimal influence for LWIR imagery. Direction labels correspond to the direction that the testbed faced, rather than the direction the aircraft flew.

3.4. Analysis

Imagery was analyzed to determine target-to-background contrast for each sensor in each illumination case. First, frames of interest were chosen at a range-to-target of 1000 m. This choice ensured ample pixels on target for each sensor, minimizing the ratio of unresolved-to-resolved pixels to ensure reasonably accurate contrast analysis. Frames were identified using a ground sample distance (GSD) range estimation method, which was validated against the GPS-labeled imagery from the first data collection. See Appendix A for a detailed discussion of this validation process and results (Tables A.1. and A.2.).

The relevant information available for a given frame included the IFOV (instantaneous field of view) of the sensor used to capture the frame; the number of pixels from one tip of the aircraft wingspan to the other; and the wingspan of the C182. Ground sample distance, or GSD, refers to the distance in meters covered by a single pixel at-range. GSD can be expressed in terms of IFOV and range-to-target as follows:

$$GSD = IFOV * R \quad \text{[meters]} \qquad [1]$$

Where the IFOV, or instantaneous field of view, is the number of milliradians spanned by a single pixel based on the size of the pixel and the focal length of the camera lens. For a given frame, the sensor IFOV, number of pixels from one tip of the C182 wingspan to the other, and the actual wingspan of the C182 (11.02 m) were known. Given this information, we can express range-to-target as:

$$R = \frac{Wingspan}{IFOV * \#\ Pixels\ Across} \quad \text{[meters]} \qquad [2]$$

After frames of interest (R = 1000 m) were identified for each sensor and illumination condition, a linear relationship between pixel gray values and equivalent reflectivity (VIS/SWIR) or equivalent blackbody temperature (MWIR/LWIR) was established. Conversion to radiometric quantities allowed direct comparison of contrast results for reflective band sensors and emissive band sensors. After radiometric conversion was established, the average signal on target and signal standard deviation were determined by carefully tracing out the aircraft as shown in Figure 3.9. The average signal of the background was determined by inverting the ROI selection, including approximately twice the number of pixels on target for the background region selection.

Figure 3.9. Region of interest on-target trace for VIS aircraft image at R = 1000 m.

After determining the average signal and signal standard deviation on target and the average background signal, RSS ΔR/ΔT was calculated for each sensor and illumination angle:

$$RSS\ \Delta R/\Delta T = \sqrt{\left(\mu_{tgt} - \mu_{bkg}\right)^2 + \sigma_{tgt}^2} \quad \text{[unitless/Celsius]} \qquad [3]$$

RSS ΔR/ΔT reflects both target-to-background contrast and on-target signal variation. This metric was chosen to better reflect the bimodal signal distribution in the VIS imagery. Moreover, study imagery showed slight blurring in the LWIR, causing the average gray value on-target in LWIR imagery to be somewhat lowered. The RSS ΔT is more robust to blur, as it accounts for the increased standard deviation of gray values caused by this slight blur, making it a better choice for contrast comparison under this condition. After calculating the RSS ΔR/ΔT for each sensor and illumination condition, results were plotted as a function of testbed vantage angle for each sensor (see Figure 3.10.). A sun icon is included in each plot to make clear the illumination angle. VIS results were plotted together, while SWIR, MWIR, and LWIR results were plotted independently.

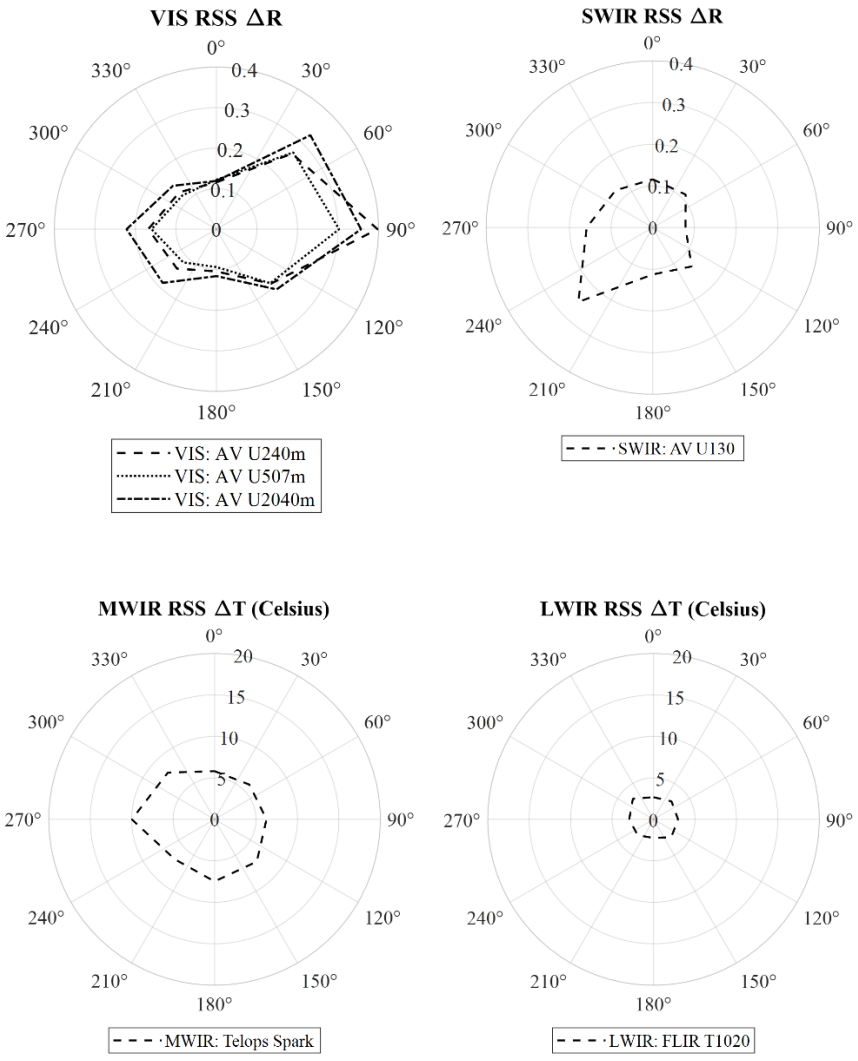

Figure 3.10. Aircraft-to-sky contrast as function of aspect angle in each band. Plots use RSS delta as a measure of target-to-background contrast and on-target signal variation.

It is worth noting that, due to small variations in flight descent rates throughout the study, plane altitude at a range of 1000 m from the sensor testbed varied slightly for each direction of approach. In other words, the aircraft's angle of elevation with respect to the horizon varied along with illumination angle (see Figure 3.11.). Because the background signal varies significantly as both a function of elevation with respect to the horizon *and* illumination angle (particularly in VIS, MWIR, and LWIR imagery), this presents a potentially confounding variable. However, the impact of elevation angle on background signal over the range of

elevations angles represented in study imagery was insignificant compared to the impact of illumination angle. So, contrast analysis assumes negligible impact of elevation angle and target-to-background contrast is described solely as a function of illumination angle. Documenting the effect of elevation with respect to horizon on background signal over EO/IR bands under relevant operating conditions is another important task for informing EO/IR design for DAA applications, but this task is beyond the scope of the current paper. Additional analysis of study data may be published in a future paper on this topic.

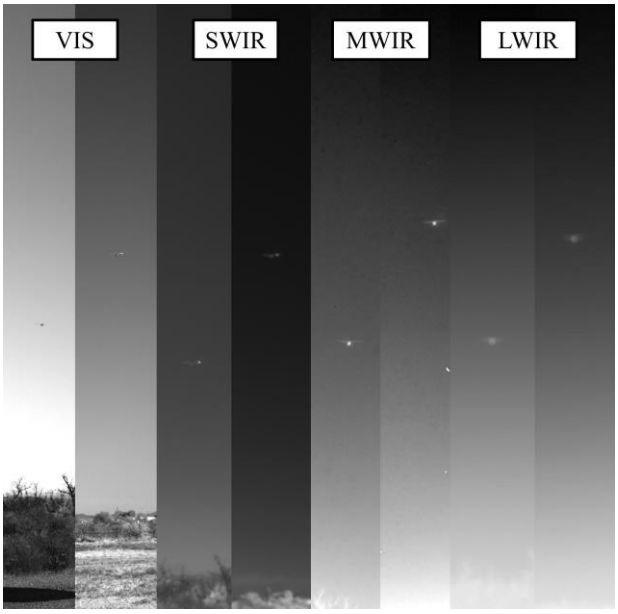

Figure 3.11. Background signal varies significantly as a function of both illumination angle *and* the elevation angle of the aircraft/background with respect to the horizon. Imagery displaying this phenomenon in the studied band is shown, with the left set of imagery showing an illumination angle of 135° and the right an angle of 315°.

Our close-range contrast measurements provided a basis for simulating long-range detection performance. The Night Vision Integrated Performance Model (NVIPM) was used to combine our measured apparent contrast values, resolution, and other sensor parameters to estimate range performance for each sensor under each illumination condition [79]. NVIPM uses the Targeting Task Performance (TTP) metric to represent the ability of an optical system to accomplish tasks

such as detection, recognition, and identification. The TTP metric takes both the sensitivity and the resolution of the imager into account. Recall the expression for TTP:

$$TTP = \int_{\xi_{low}}^{\xi_{cut}} \left[\frac{C_{tgt}}{CTF_{sys}(\xi)}\right]^{\frac{1}{2}} \qquad \text{[cycles/mr]} \qquad [4]$$

ξ_{cut} and ξ_{low} are the highest and lowest spatial frequencies in the scene, C_{TGT} is the target's contrast, and $CTF_{sys}(\xi)$ is the system contrast threshold function. The CTF of the system describes which frequencies can make it through the system and be detected by the human eye, as contrast is degraded at higher spatial frequencies. Recall the expression for $CTF_{sys}(\xi)$:

$$CTF_{sys}(\xi) = \frac{CTF_{eye}(\xi)}{MTF(\xi)}\left(1 + \frac{\alpha^2\sigma^2(\xi)}{SCT^2}\right)^{\frac{1}{2}} \quad \text{[unitless]} \qquad [5]$$

where $CTF_{eye}(\xi)$ is the eye contrast threshold function and $MTF(\xi)$ is the modulation transfer function of the system, which measures an imaging system's resolution in terms of the spatial frequencies it can transmit. The second half of equation 5 describes the sensitivity of the imager. SCT is the scene contrast temperature and describes the range of radiant flux to which an imager is sensitive. $\sigma(\xi)$ is the noise filtered by the display in Kelvin-root seconds and α is a proportionality factor (169.6 root-Hertz).

Once the TTP is calculated, the result can be compared to the V-number corresponding to a specific task, generating the probability of accomplishing that task at a certain TTP value. V-numbers are based on human perception experiments, since human perception still represents the gold standard in terms of signal processing [70].

In NVIPM, detailed camera specifications were imported for the six cameras, each in a different file. For each file, target and background data differed based on the illumination condition for the measured contrast. To reflect this, each sensor simulation was looped over target and background measurements for the eight illumination angles observed.

The typical V-number used for a detection task is V = 2. This was determined by perception experiments where humans attempt to detect a target against the ground. This application is

slightly different because detection against a mostly uniform sky is an “easier” task to accomplish than detection against the ground. To revise the V-number for detection against the sky, V-number was correlated against the chosen metric of 4 pixels-on-target with a very high contrast, as suggested by our research sponsor. When inputting a target with high contrast, the V-number corresponding to 80% probability of detection (this is the standard for good probability of detection) was found at the range where the target covered four pixels of the imager. Table 3 shows the results for each sensor.

Table 3.3. V-number corresponding to high contrast 4 pixels-on-target for each sensor

Sensor	V-number
VIS U-240	1.03
VIS U-507	1
VIS U-2040	0.91
SWIR	1.11
MWIR	1.08
LWIR	0.96

Based on these results, V = 1 was chosen as the representative V-number for detection against the sky. For each model, the range for 80% probability of detection is calculated using V = 1 in both a desert and a maritime atmosphere. NVIPM uses MODTRAN to calculate the effect of different atmospheres on imaging performance. Figure 3.12. shows the results of this analysis for desert and maritime atmospheres.

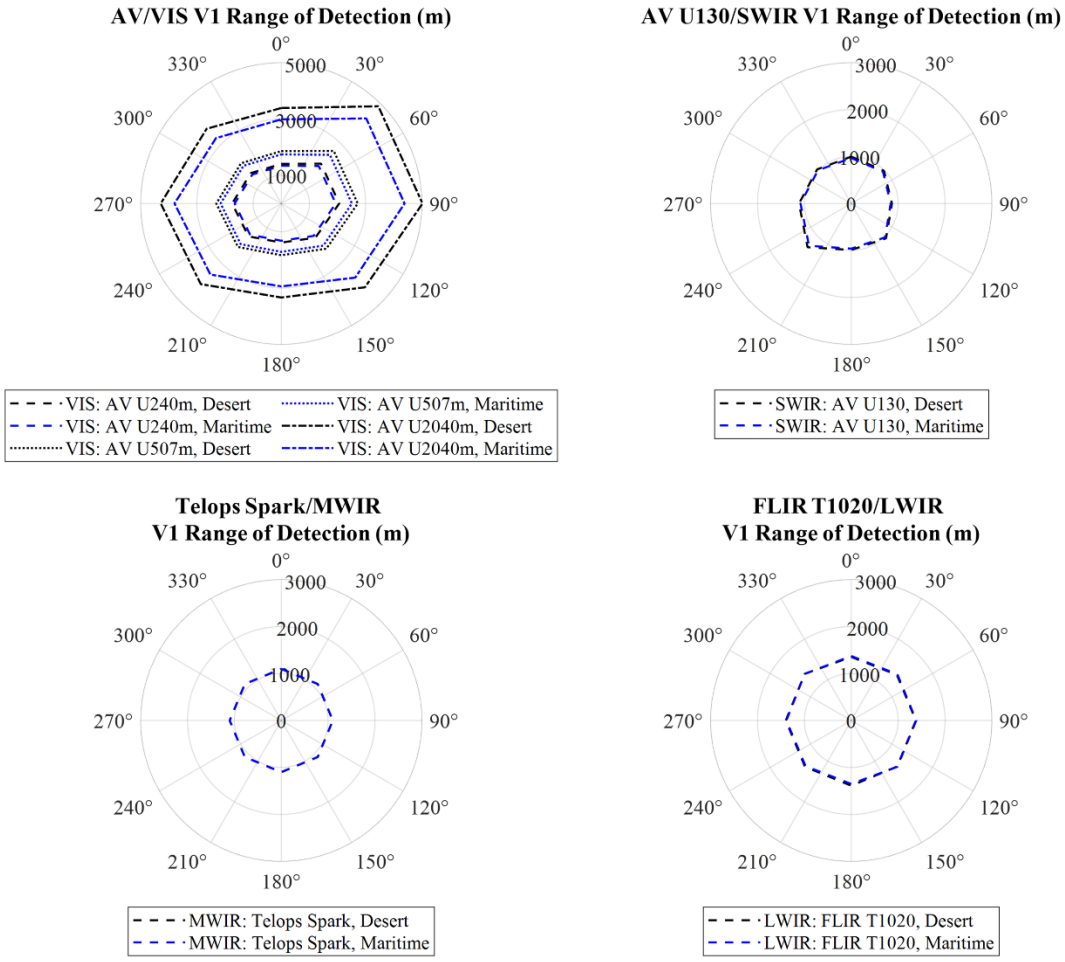

Figure 3.12. Range performance simulation results for desert and maritime atmospheres. Range performance estimate accounts for degradation of signal as it propagates (MODTRAN) and combines contrast and resolution parameters to estimate range of detection (NVIPM).

3.5. Discussion

As expected, the reflective band sensors (VIS and SWIR) saw strong variations in target-to-background contrast as a function of illumination angle. VIS imagery displayed a bimodal target signal for all illumination angles, meaning that there were two spikes in the signal histogram: one bright and one dark. This bimodal signal was caused by VIS radiation conveying information

about the varied colors of aircraft material (metal, paint, glass, etc.). Imagery of the directly illuminated and backlit aircraft (90º and 270º) showed the strongest contrast, with the directly illuminated aircraft showing positive contrast and the backlit aircraft showing negative contrast. The contrast reversal between direct illumination and backlit illumination suggests low target-to-background contrast at oblique illumination angles (0º and 180º), which may create detection difficulties for long-range imagery with few pixels on target. Despite low contrast in average signal at these angles, on-target signal variations still provided detectable signal, as suggested by the non-zero RSS-delta results.

While aircraft-to-sky contrast also varied significantly as a function of illumination angle in the SWIR imagery, contrast remained positive across all illumination angles. The target signal was bright over the entire target in each image analyzed, suggesting minimal dependence of SWIR signal on varying material colors or types. The strongest contrast case for SWIR appeared in the SW-facing imagery (225º). Reviewing the corresponding image (see Figure 3.8.) shows that the contrast outlier reflected a strong signal from the aircraft signal light, or perhaps from glare off the glass window covering the light. Barring this outlier data point, SWIR imagery of the directly illuminated aircraft showed the highest contrast. This vantage maximized the brightness of the target signal and minimized background sky path radiance. The weakest contrast appeared in the backlit imagery, which minimized the brightness of the target signal and maximized background sky path radiance. Overall, SWIR imagery aircraft-to-sky contrast was low relative to contrast in VIS imagery.

Aircraft-to-sky contrast in MWIR imagery showed minor dependence on illumination angle, with similar results to SWIR imagery, showing lower contrast for the backlit aircraft and higher contrast for the directly illuminated aircraft. This minor dependence was expected, as MWIR sensors record some reflected radiation as well as emissive radiation. Aircraft-to-sky contrast in LWIR imagery showed no significant dependence on illumination angle and the same positive contrast as SWIR and MWIR imagery. Contrast in the LWIR band appeared much weaker than in MWIR.

Slight variations in aircraft-to-sky contrast could be seen in the RSS-delta results for the LWIR imagery, and these variations were explained by small differences in aircraft altitude for imagery at each angle for a range-to-target of 1000 m. Differences in altitude across imagery in all bands slightly affected the contrast analysis, but the influence of altitude was insignificant relative to the influence of illumination angle for all cases except the LWIR. Still, this result raises an important point: imager performance will vary significantly as a function of the relative altitude of the UAV on which a detection avoidance imager is mounted and any aircraft which is a non-cooperative collision risk. Sky near the horizon appears much brighter in all bands studied (VIS, SWIR, MWIR, and LWIR) than sky further from the horizon.

The results of the contrast study showed that VIS and MWIR imagers were most sensitive to the signal of the C-182 aircraft against a clear-sky background in a desert atmosphere. The NVIPM analysis took this result and considered the combined effect of sensor sensitivity and resolution to simulate the range performance of each imager for the task of aircraft detection. It is important to understand the simulation results were particular to the sensors chosen for this study, and these sensors were chosen primarily for the task of comparing the sensitivity of each band to the signal of the aircraft against the clear sky rather than for maximizing resolution or range performance.

Both the desert and maritime atmosphere simulations showed that the VIS sensors would expect the best range performance in most cases, with the higher resolution sensors detecting at longer ranges. At oblique illumination angles (0º and 180º), the low-resolution VIS sensor was estimated to perform similarly to the LWIR sensor. The next best performer was the LWIR sensor (1024 by 786 pixels), offering a longer detection range than the more sensitive but lower resolution MWIR sensor (640 by 512 pixels) and the less sensitive but higher resolution SWIR sensor (1280 by 1024 pixels). The difference in performance between desert and maritime atmospheres was minimal for the SWIR, MWIR, and LWIR sensors. There was some degradation to range performance in the VIS for the maritime atmosphere. This aligns with theoretical expectations, as VIS shows significantly reduced range performance under degraded atmospheric conditions (like high water content, as in a maritime atmosphere) relative to longer wavelength bands like SWIR, MWIR, and LWIR. Still, the VIS sensors' higher resolution detectors mostly outperformed the SWIR, MWIR, and LWIR sensors by a significant margin.

The MWIR sensor used in the study was the lowest resolution by far, and it can be expected that using a MWIR detector of a similar resolution to the LWIR and SWIR sensors used would outperform these sensors and the low-resolution VIS sensor at oblique angles, if not also the moderate resolution VIS.

In summary, the contrast of the studied Cessna 182 aircraft against a clear sky in a desert atmosphere was found to be strongest in VIS and MWIR imagery, considering variations in target and background signal due to illumination and target characteristics. The advantage of MWIR over VIS was its consistently high and positive contrast, whereas VIS displayed a contrast reversal at oblique illumination angles which may pose difficulties for long-range detection. VIS performance may degrade or improve for different colored aircraft and in water-rich atmospheres. These factors make VIS a less reliable choice for the task of aircraft detection than MWIR from the perspective of imager sensitivity to aircraft signal. However, the relative affordability, accessibility, and low-SWAP of VIS sensors compared to MWIR sensors make VIS a potentially suitable choice for an aircraft collision avoidance system on a small- to mid-size UAV system. The two sensors may also be used in tandem to increase system performance and flexibility. Many aviation EO/IR gimbals include both VIS and MWIR sensors. These gimbals may be strong candidates for adaptation to DAA surveillance.

Choice of imaging band for the EO/IR component of a DAA system may also be informed by system specific requirements on minimum detection range, UAV SWAP capacity, and operation environment (low- versus high-altitude, urban versus rural, etc.). For systems with the capacity to perform initial detection at long range, such as those that employ acoustic sensors, variable FOV and scanning capabilities for the EO/IR system may be beneficial. This would increase the range performance of the EO/IR system and enable utility immediately after initial detection.

The collection of additional aircraft-to-background contrast data for EO/IR sensors across bands of interest, for different targets, and under various illumination, atmospheric, and background conditions would greatly support the informed design of DAA sensors for UAV operations. Moreover, this data would be invaluable to testing and developing detection algorithms with real EO/IR imagery. Due to these benefits, additional research may be pursued comparing EO/IR

band performance at night, at and below the horizon line (high path radiance sky and ground or sea backgrounds), and under different atmospheric and weather conditions. Research on the use of zoom capable EO/IR sensors alongside other initial detection instruments, such as acoustic sensors, may also be beneficial to optimizing the optical design of EO/IR sensors for the task of aircraft collision avoidance.

CONCLUSION

This study suggests that the VIS and MWIR sensors provide stronger aircraft-to-sky contrast than do SWIR and LWIR sensors under clear sky and daytime illumination conditions. The availability and affordability of high resolution, low-SWAP VIS sensors make them a strong choice for aircraft collision avoidance systems, while the consistent positive contrast and lower dependence on illumination angle and aircraft characteristics are strong benefits for MWIR imagery. MWIR imagery also may perform better under degraded atmospheric conditions due to its sensitivity to longer wavelengths. Due to their differing strengths, VIS and MWIR sensors may be fused to create a high performing and adaptable EO/IR detect and avoid system.

Range performance simulations based on contrast study results showed that the resolution of the EO/IR detector remains critical to the minimum range of detection, with the low-resolution MWIR sensor performing the worst out of all study sensors despite strong sensitivity to the aircraft signal. One solution to the limit imposed by detector resolution may be the use of optical zoom. Additional research may be performed investigating the use of zoom-capable scanning EO/IR sensors for collision avoidance.

This study serves as an initial investigation into aircraft-to-background contrast for the purpose of EO/IR design for aircraft collision avoidance, providing a method for collecting calibrated EO/IR sensitivity data under varied illumination conditions. Interpretability of study results would improve greatly with further research into aircraft-to-background contrast during the night, for near- and below-horizon imagery, with various ground and sea backgrounds, and under different weather and atmosphere conditions. The systematic and rigorous collection of imagery under these conditions will be invaluable to developing, testing, and validating the performance of EO/IR sensors and detection algorithms under diverse conditions for UAV-based DAA systems.

APPENDIX A.

Additional Figures and Tables

Appendix A. includes supplemental tables and figures that were omitted from the main body of the thesis, but which still ought to be available for reference and examination.

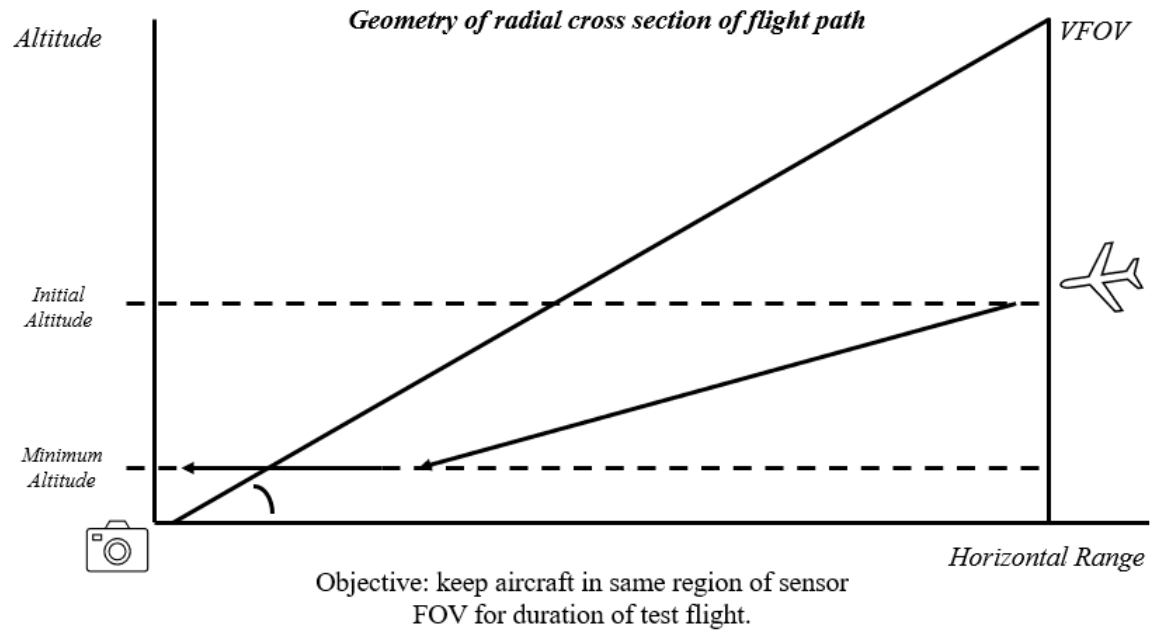

Figure A.1. During the test flight, the pilot was directed to begin a gradual and even descent when they reached 3000 m from the testbed, ending at approximately 200 m above ground level when 500 m from the testbed. This flight pattern was repeated for approaches over all cardinal and ordinal directions.

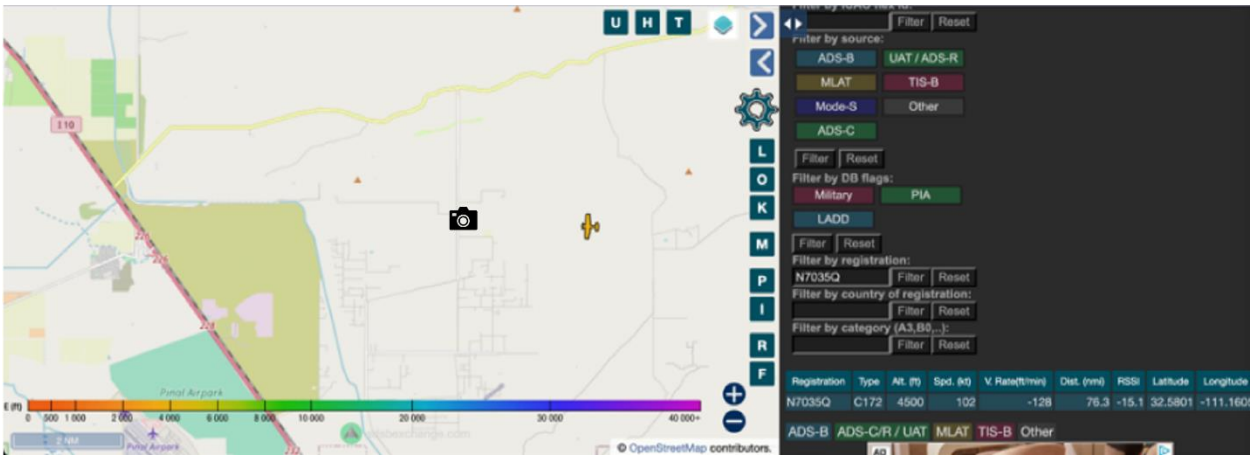

Figure A.2. Screenshot of ADS-B data as-recorded throughout test flight. Timestamps on recording were correlated with timestamps on recorded imagery, allowing each image to be associated with a corresponding GPS reading on the aircraft.

Tables A.1. and A.2. provide information used to identify the frames of interest for the contrast study. The initial study (Marana) used ADS-B data to track aircraft, and GPS data from ADS-B measurements were tagged to the corresponding imagery via synchronized timestamps. During the second study (Picture Rocks), the study aircraft was broadcasting ADS-B data on an unexpected frequency, and so it was not recorded. To identify frames at 1000 m range for the contrast study, a ground sample distance-based (GSD) method was used. This method was first validated against the GPS-tagged data to ensure accuracy at a range of 1000 m.

Table A.1. shows the testbed sensors, each of their IFOVs, the corresponding GSD at 1000 m, and the number of pixels expected across the 11-meter wingspan of the C182 aircraft. Table A.2. shows a comparison between GSD-based range estimation and GPS-based range measurements for the high-resolution visible imagery. Results show that the GSD method consistently estimates the plan to be 100 m closer to the sensor than do ADS-B GPS measurements. This discrepancy is expected given aircraft speed of 50 to 75 m/s and ADS-B delay of 1 to 2 seconds.

Table A.1. GSD at 1000 m and pixels-across-wingspan calculations for testbed sensors

Sensors	V U240m	V U507m	V U2040m	VSWIR	MWIR	LWIR
IFOV (mrad)	0.2875	0.2156	0.1096	0.4167	0.6000	0.4860
GSD at 1000 m (m)	0.2875	0.2153	0.1096	0.4167	0.6000	0.4860
Pixels across wingspan	38	51	101	26	18	23

Table A.2. Comparison between GPS-based and GSD-based range estimation

Frame Number	Frame 1: 8:54:45 am[a]	Frame 2: 8:54:55 am	Frame 3: 8:55:05 am	Frame 4: 8:55:15 am	Frame 5: 8:55:25 am	Frame 6: 8:55:34 am
Expected # Pixels	43	54	67	93	158	530
Actual # Pixels	45	57	75	103	184	436
GPS Range (m)	2323	1852	1476	1071	627	187
GSD Range (m)	2200	1740	1322	960	540	227

[a]Timestamps refer to time of capture from Marana test flight.

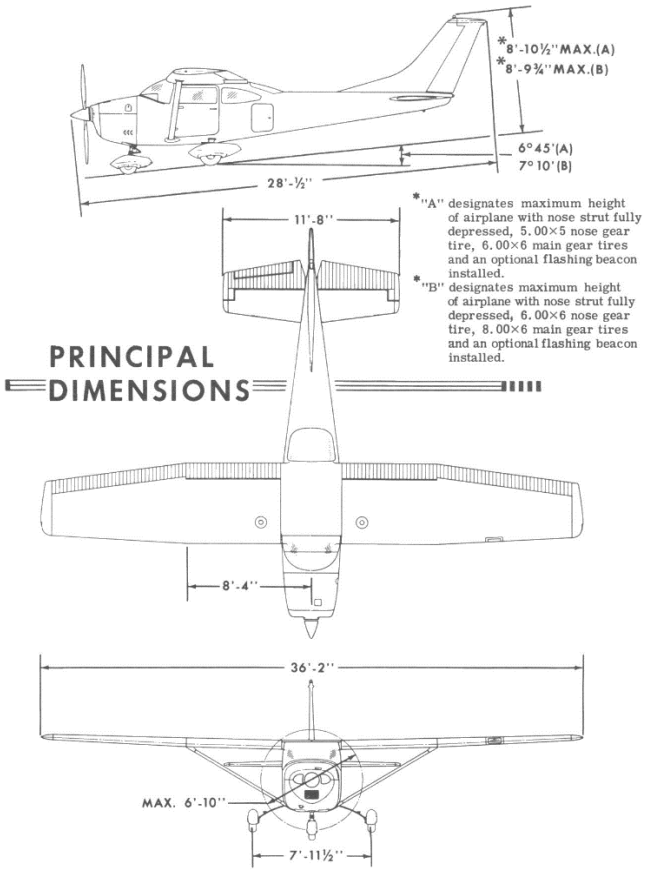

Figure A.3. [Left] Principal dimensions of C-182, which were used to calculate target characteristic dimension in pixel on target calculations and range performance simulations.

[Right] Photograph of C-182 aircraft flown for contrast study.

REFERENCES

[1] Roessger, E. (1958). A History of the Air Collision Problem. *The Journal of Navigation*, *11*(1), 14–17. https://doi.org/10.1017/S0373463300017276

[2] Kraus, T. L. (2008). Prologue. In *The Federal Aviation Administration: A Historical Perspective, 1903—2008*. The Federal Aviation Administration.

[3] Gilbert, G. (1973). Historical Development of the Air Traffic Control System. *IEEE Transactions on Communications*, *21*(5), 364–375. https://doi.org/10.1109/TCOM.1973.1091699

[4] Kraus, T. L. (2008). Birth of the FAA. In *The Federal Aviation Administration: A Historical Perspective, 1903—2008*. The Federal Aviation Administration.

[5] Tymms, F. (1970). ICAO—Its Origin and Development: A Personal View. *The Aeronautical Journal*, *74*(712), 269–279. https://doi.org/10.1017/S0001924000047564

[6] Kraus, T. L. (2008). New Challenges – New Duties. In *The Federal Aviation Administration: A Historical Perspective, 1903—2008*. The Federal Aviation Administration.

[7] Shuch, H. P. (1989). General Aviation Collision-Avoidance Alternatives. *Journal of Transportation Engineering*, *115*(5), 474–492. https://doi.org/10.1061/(ASCE)0733-947X(1989)115:5(474)

[8] Walsh, J., & Wojciech, J. (1991). TCAS in the 1990s. *NAVIGATION*, *38*(4), 383–397. https://doi.org/10.1002/j.2161-4296.1991.tb01870.x

[9] Mba Andeme, J. M. N., Liu, Q., & Hadi, A. (2021). FAA Transition Away from Radar and Towards ADS-B Aircraft Communication-Based on Accuracy. In Y. Tan, Y. Shi, A. Zomaya, H. Yan, & J. Cai (Eds.), *Data Mining and Big Data* (pp. 358–374). Springer. https://doi.org/10.1007/978-981-16-7502-7_35

[10] Strohmeier, M., Schäfer, M., Lenders, V., & Martinovic, I. (2014). Realities and challenges of NextGen air traffic management: The case of ADS-B. *IEEE Communications Magazine*, *52*(5), 111–118. https://doi.org/10.1109/MCOM.2014.6815901

[11] Rawat, S. (n.d.). *Air Traffic Control (ATC) Transponder*. Study Aircrafts. Retrieved March 5, 2024, from https://www.studyaircrafts.com/atc-transponder

[12] Kochenderfer, M. J., Holland, J. E., & Chryssanthacopoulos, J. P. (2012). Next-Generation Airborne Collision Avoidance System. *Lincoln Laboratory Journal*.

[13] Kraus, T. L. (2008). A System in Turmoil. In *The Federal Aviation Administration: A Historical Perspective, 1903—2008*. The Federal Aviation Administration.

[14] Smith, M., Strohmeier, M., Harman, J., Lenders, V., & Martinovic, I. (2020, February 24). *A View from the Cockpit: Exploring Pilot Reactions to Attacks on Avionic Systems*. https://doi.org/10.14722/ndss.2020.23022

[15] Yanovsky, F. J. (2013). *Autonomous Radio Sensors for Motion Parameters* (pp. 89–136). https://doi.org/10.13140/RG.2.1.5158.8640

[16] Kraus, T. L. (2008). Getting Ready for NextGen. In *The Federal Aviation Administration: A Historical Perspective, 1903—2008*. The Federal Aviation Administration.

[17] UAV Navigation. (n.d.). *Transponder ADS-B Integration*. Retrieved February 18, 2024, from https://www.uavnavigation.com/company/news-and-events/transponder-ads-b-integration

[18] Tamimi, A., Hahn, A., & Roy, S. (2020). Cyber Threat Impact Analysis to Air Traffic Flows Through Dynamic Queue Networks. *ACM Transactions on Cyber-Physical Systems*, *4*(3), 1–22. https://doi.org/10.1145/3377425

[19] Yim, W. F. (2014). The Next Generation of Air Transportation System (NextGEN). *Challenges and Advances in Sustainable Transportation Systems*, 25–32. https://doi.org/10.1061/9780784413364.004

[20] Hobbs, A. (2010). Unmanned Aircraft Systems. In E. Salas & D. Maurino (Eds.), *Human Factors in Aviation (Second Edition)* (pp. 505–531). Academic Press. https://doi.org/10.1016/B978-0-12-374518-7.00016-X

[21] Keane, J. F., & Carr, S. S. (2013). A Brief History of Early Unmanned Aircraft. *JOHNS HOPKINS APL TECHNICAL DIGEST*, *32*(3).

[22] Daly, D. (2020). *A Not-So-Short History of Unmanned Aerial Vehicles (UAV)*. Consortiq. https://consortiq.com/uas-resources/short-history-unmanned-aerial-vehicles-uavs

[23] Polijak, M. (2019). *The History Of Drones: From 1907 to 2023*. Drone Tech Planet. https://www.dronetechplanet.com/the-history-of-drones-timeline-from-1907-to-2019/

[24] Canis, B. (n.d.). Unmanned Aircraft Systems (UAS): Commercial Outlook for a New Industry. *Unmanned Aircraft Systems*.

[25] Kopardekar, P., Rios, J., Prevot, T., Johnson, M., Jung, J., & Robinson III, J. E. (2016). UAS Traffic Management (UTM) Concept of Operations to Safely Enable Low Altitude Flight Operations. In *16th AIAA Aviation Technology, Integration, and Operations*

Conference. American Institute of Aeronautics and Astronautics. https://doi.org/10.2514/6.2016-3292

[26] Bellows, B. (2013). Floating toward a Sky Near You: Unmanned Aircraft Systems and the Implications of the FAA Modernization and Reform Act of 2012. *Journal of Air Law and Commerce*, *78*, 585.

[27] Federal Aviation Administration. (2016). 14 CFR Part 107, Docket FAA-2015-0150, Amdt. 107-1, 81 FR 42209. National Archives.

[28] Blake, T. (2021). *What is Unmanned Aircraft Systems Traffic Management?* [NASA]. https://www.nasa.gov/centers-and-facilities/ames/what-is-unmanned-aircraft-systems-traffic-management/

[29] Gipson, L. (2016). *UAS Integration in the NAS Project*. https://www.semanticscholar.org/paper/UAS-Integration-in-the-NAS-Project-Gipson/12d7208b7542d345bf5c607aad69d87f91adc1e5

[30] *NASA Advanced Air Mobility: Ecosystem Working Groups Portal*. (n.d.). NASA Aeronautics Research Institute. Retrieved March 6, 2024, from https://nari.arc.nasa.gov/aam-portal/

[31] Code of Federal Regulations. (1967). 14 CFR Part 91—General Operating and Flight Rules. National Archives. https://www.ecfr.gov/current/title-14/part-91

[32] Federal Aviation Administration. (1983). AC 90-48C - Pilots' Role in Collision Avoidance (Cancelled). FAA. https://www.faa.gov/regulations_policies/advisory_circulars/index.cfm/go/document.information/documentID/23090

[33] International Civil Aviation Organisation (ICAO). (2005). Rules of the Air: Annex 2. The Convention on International Civil Aviation.

[34] Radio Technical Commission for Aeronautics (RTCA). (2020). DO-366—Minimum Operational Performance Standards (MOPS) for Air-to-Air Radar for Traffic Surveillance. GlobalSpec. https://standards.globalspec.com/std/14562761/DO-365C

[35] Radio Technical Commission for Aeronautics (RTCA). (2022). DO-365C - Minimum Operational Performance Standards (MOPS) for Detect and Avoid (DAA) Systems. GlobalSpec. https://standards.globalspec.com/std/14562761/DO-365C

[36] ASTM International. (2022). F3411-22A: Standard Specification for Remote ID and Tracking. ASTM International.

[37] Cone, A. C., Wu, M. G., & Lee, S. M. (2019). Detect-and-Avoid Alerting Performance for High-Speed UAS and Non-Cooperative Aircraft. AIAA Aviation 2019 Forum. AIAA Aviation 2019 Forum, Dallas, Texas. https://doi.org/10.2514/6.2019-3313

[38] Monk, K., Rorie, R. C., Keeler, J., & Sadler, G. (2020). An Examination of Two Non-Cooperative Detect and Avoid Well Clear Definitions. In AIAA AVIATION 2020 FORUM. American Institute of Aeronautics and Astronautics. https://doi.org/10.2514/6.2020-3263

[39] Wu, M. G., Lee, S., Serres, C. C., Gill, B., Edwards, M. W. M., Smearcheck, S., Adami, T., & Calhoun, S. (2020). Detect-and-Avoid Closed-Loop Evaluation of Noncooperative Well Clear Definitions. Journal of Air Transportation, 28(4), 195–206. https://doi.org/10.2514/1.D0199

[40] Peinecke, N. (2022). How to stay well clear in corridors and swarms: Detect-and-avoid ranges for geovectoring concepts. 2022 International Conference on Unmanned Aircraft Systems (ICUAS), 57–63. https://doi.org/10.1109/ICUAS54217.2022.9836220

[41] Loffi, J. M., Vance, S. M., Jacob, J., Spaulding, L., & Dunlap, J. C. (2022). Evaluation of Onboard Detect-and-Avoid System for sUAS BVLOS Operations. International Journal of Aviation, Aeronautics, and Aerospace. https://doi.org/10.15394/ijaaa.2022.1701

[42] Nex, F., Armenakis, C., Cramer, M., Cucci, D. A., Gerke, M., Honkavaara, E., Kukko, A., Persello, C., & Skaloud, J. (2022). UAV in the advent of the twenties: Where we stand and what is next. ISPRS Journal of Photogrammetry and Remote Sensing, 184, 215–242. https://doi.org/10.1016/j.isprsjprs.2021.12.006

[43] International Civil Aviation Organisation (ICAO). (2011). Cir 328 AN/190, Unmanned Aircraft Systems (UAS). International Civil Aviation Organization. https://www.icao.int/Meetings/UAS/Documents/Circular%20328_en.pdf

[44] Radio Technical Commission for Aeronautics (RTCA). (2013). DO-344—Operational and Functional Requirements and Safety Objectives (OFRSO) for Unmanned Aircraft Systems (UAS) Standards. GlobalSpec. https://standards.globalspec.com/std/14562761/DO-365C

[45] Albaker, B. M., & Rahim, N. A. (2009). A survey of collision avoidance approaches for unmanned aerial vehicles. 2009 International Conference for Technical Postgraduates (TECHPOS), 1–7.

[46] Hottman, S. B., Hansen, K. R., & Berry, M. (2009). Literature Review on Detect, Sense, and Avoid Technology for Unmanned Aircraft Systems. U.S. Department of Transportation.

[47] ASTM International. (2017). F2411-04: Standard Specification for Design and Performance of an Airborne Sense-and-Avoid System. ASTM International.

[48] Zeitlin, A. (2006). Collision Avoidance for Unmanned Aircraft: Proving the Safety Case. The MITRE Corporation and MIT Lincoln Laboratory.

[49] Albaker, B. M., & Rahim, N. A. (2010). Unmanned aircraft collision detection and resolution: Concept and survey. 2010 5th IEEE Conference on Industrial Electronics and Applications, 248–253. https://doi.org/10.1109/ICIEA.2010.5516808

[50] Masutti, A. (2009). Proposals for the Regulation of Unmanned Air Vehicle Use in Common Airspace. Air and Space Law, 34(1). https://kluwerlawonline.com/api/Product/CitationPDFURL?file=Journals\AILA\AILA2009001.pdf

[51] Stöcker, C., Bennett, R., Nex, F., Gerke, M., & Zevenbergen, J. (2017). Review of the Current State of UAV Regulations. Remote Sensing, 9(5), Article 5. https://doi.org/10.3390/rs9050459

[52] Minwalla, C., & Ellis, K. (2017). Experimental Evaluation of PICAS: An Electro-Optical Array for Non-Cooperative Collision Sensing on Unmanned Aircraft Systems. AIAA Information Systems-AIAA Infotech @ Aerospace, Grapevine, Texas. https://doi.org/10.2514/6.2017-0907

[53] Oliveros, E. V., & Murray, A. J. (2010). Modeling and Simulation of an UAS Collision Avoidance Systems. https://ntrs.nasa.gov/citations/20100042541

[54] Maltese, D., & Farjon, J. (2020). Detect and avoid function for UAVs: Presentation of an EO/IR sensor solution. Infrared Technology and Applications XLVI, 11407, 115–129. https://doi.org/10.1117/12.2559461

[55] Temizer, S., Kochenderfer, M., Kaelbling, L., Lozano-Perez, T., & Kuchar, J. (2010). Collision Avoidance for Unmanned Aircraft using Markov Decision Processes. AIAA Guidance, Navigation, and Control Conference, Toronto, Ontario, Canada. https://doi.org/10.2514/6.2010-8040

[56] Portilla, E., Fung, A., Chen, W.-Z., Shakernia, O., & Molnar, T. (2007). Sense And Avoid (SAA) & Traffic Alert and Collision Avoidance System (TCAS) Integration for Unmanned Aerial Systems (UAS). AIAA 2007 Conference and Exhibit, Rohnert Park, California. https://doi.org/10.2514/6.2007-3004

[57] Carnie, R., Walker, R., & Corke, P. (2006). Image processing algorithms for UAV "sense and avoid." Proceedings 2006 IEEE International Conference on Robotics and Automation, 2006. ICRA 2006., 2848–2853. https://doi.org/10.1109/ROBOT.2006.1642133

[58] Mukherjee, A., Mondal, S., & Tsourdos, A. (2024). Autonomous Detect and Avoid algorithm respecting airborne Right of Way rules. AIAA SCITECH 2024 Forum. https://doi.org/10.2514/6.2024-1080

[59] Zitar, R. A., Al-Betar, M., Ryalat, M., & Kassaymeh, S. (2023). A review of UAV Visual Detection and Tracking Methods (arXiv:2306.05089). arXiv. https://doi.org/10.48550/arXiv.2306.05089

[60] Fraga-Lamas, P., Ramos, L., Mondéjar-Guerra, V., & Fernández-Caramés, T. M. (2019). A Review on IoT Deep Learning UAV Systems for Autonomous Obstacle Detection and Collision Avoidance. Remote Sensing, 11(18), Article 18. https://doi.org/10.3390/rs11182144

[61] Butt, M. Z., Nasir, N., & A. Rashid, R. B. (2024). A review of perception sensors, techniques, and hardware architectures for autonomous low-altitude UAVs in non-cooperative local obstacle avoidance. Robotics and Autonomous Systems, 173, 104629. https://doi.org/10.1016/j.robot.2024.104629

[62] Rouhi, A., Arezoomandan, S., Kapoor, R., Klohoker, J., Patal, S., Shah, P., Umare, H., & Han, D. (2024). An Overview of Deep Learning in UAV Perception. 2024 IEEE International Conference on Consumer Electronics (ICCE), 1–6. https://doi.org/10.1109/ICCE59016.2024.10444237

[63] Lee, J., Hwang, S., & Hyunchul Shim, D. (2018). Consideration of Airborne Detection System for DAA Technology in Remote Pilot Aircraft Systems. 2018 IEEE/AIAA 37th Digital Avionics Systems Conference (DASC), 1–5. https://doi.org/10.1109/DASC.2018.8569841

[64] Griffith, J., Kochenderfer, M., & Kuchar, J. (2012). Electro-Optical System Analysis for Sense and Avoid. In AIAA Guidance, Navigation and Control Conference and Exhibit. American Institute of Aeronautics and Astronautics. https://doi.org/10.2514/6.2008-7253

[65] Ganguli, A., Avadhanam, S., Bai, H., Yadegar, J., Utt, J., & McCalmont, J. (2011). Multiple intruder tracking using a laser enhanced EO/IR Sense and Avoid system. Infotech@Aerospace 2011, St. Louis, Missouri. https://doi.org/10.2514/6.2011-1478

[66] Contarino, M. (2010). All weather collision avoidance for unmanned aircraft systems. Unmanned Systems Technology XII, 7692, 13–21. https://doi.org/10.1117/12.850248

[67] Verstraeten, J., Stuip, M., & Birgelen, T. van. (2015). Assessment of Detect and Avoid Solutions for Use of Unmanned Aircraft Systems in Nonsegregated Airspace. In K. P. Valavanis & G. J. Vachtsevanos (Eds.), Handbook of Unmanned Aerial Vehicles (pp. 1955–1979). Springer Netherlands. https://doi.org/10.1007/978-90-481-9707-1_70

[68] Valenta, C. R., & Silva, Z. J. (2020). Towards single aperture RF/EO/IR systems: Multi-spectral sensing and communication (Rising Researcher). Laser Radar Technology and Applications XXV, 11410, 68–82. https://doi.org/10.1117/12.2558096

[69] Snarski, S., Barnes, R., Khan, N., Baker, J., & Webb, J. (2022). Infrared search and track (IRST) for long-range, wide-area detect and avoid (DAA) on small unmanned aircraft systems (sUAS). Autonomous Systems: Sensors, Processing and Security for Ground, Air, Sea and Space Vehicles and Infrastructure 2022, 12115, 21–40. https://doi.org/10.1117/12.2618065

[70] Driggers, R. G., Friedman, M. H., Devitt, J. W., Furxhi, O., & Singh, A. (2022). Introduction to Infrared and Electro-optical Systems (3rd edition). Artech House.

[71] Wiley, L., Follansbee, J., Leslie, P., Furxhi, O., Pimpinella, R., Brady, D., & Driggers, R. (2022). Target discrimination in the extended shortwave infrared band (2 to 2.5μm) compared with visible, near-infrared, and SWIR in degraded visual environments. Optical Engineering, 61(11), 113103. https://doi.org/10.1117/1.OE.61.11.113103

[72] Driggers, R. G., Hodgkin, V., & Vollmerhausen, R. (2013). What good is SWIR? Passive day comparison of VIS, NIR, and SWIR (G. C. Holst & K. A. Krapels, Eds.; p. 87060L). https://doi.org/10.1117/12.2016467

[73] Dudzik, M. C., Accetta, J. S., & Shumaker, D. L. (1993). Infrared & Electro-Optical Systems Handbook. Electro-Optical Systems Design, Analysis, and Testing, Volume 4. (ADA364024). Infrared Information and Analysis Center, Ann Arbor, MI. https://ntrl.ntis.gov/NTRL/dashboard/searchResults/titleDetail/ADA364024.xhtml

[74] Infrared Sensors for Space | Teledyne Imaging. (n.d.). Retrieved March 10, 2024, from https://www.teledyneimaging.com/en/aerospace-and-defense/products/infrared-sensors-for-space/

[75] Holst, G. C. (2007). Imaging system performance based upon F/d. Optical Engineering, 46(10), 103204. https://doi.org/10.1117/1.2790066

[76] Ferguson, A. (2018). Pathfinder Focus Area 2: Phase III Report. Federal Aviation Administration (FAA). https://www.faapathfinderreport.com/

[77] Schmidt, L. M., Conway, B., DePoy, D. L., Marshall, J. L., & Oelkers, R. J. (2022). Reflectivity characterization of various black and white materials. Advances in Optical and Mechanical Technologies for Telescopes and Instrumentation V, 12188, 1537–1543. https://doi.org/10.1117/12.2630244

[78] Edmund Optics. (n.d.). Pre-mix white reflectance coating. https://www.edmundoptics.com/f/ pre-mix-white-reflectance-coating/11427

[79] Teaney, B. P., & Haefner, D. P. (2016). Measured system component development for the night vision integrated performance model (NV-IPM) (G. C. Holst & K. A. Krapels, Eds.; p. 982007). https://doi.org/10.1117/12.2224734